![AIAA logo]

Film-Cooling Experiments in a Vane Cascade with Cylindrical and Diffused-Cylindrical Holes in Upstream Endwall

Journal:	*Journal of Thermophysics and Heat Transfer*
Manuscript ID	2022-03-T6607.R2
Manuscript Type:	Full Paper
Date Submitted by the Author:	n/a
Complete List of Authors:	Huyssen, Barbara; University of Pretoria, and aeronautical engineering Shote, Adeola; University of Pretoria, Mechanical & Aeronautical Engineering MAHMOOD, GAZI; University of Pretoria, Mechanical & Aeronautical Engineering
Subject Index Category:	60910 Gas Turbine Engines < 60000 PROPULSION, 60630 Engine Cooling and Heat Transfer < 60000 PROPULSION

SCHOLARONE™
Manuscripts

Wruvtgco 'Gpf ycmlHko /Eqqkpi 'kp't'Xcpg'Ecuecfg'ykj "

E{rkpftlecnlUjcrg'Jqngu

Barbara B. Huyssen[1], Adeola S. Shote[1], and Gazi I. Mahmood[2,*]
University of Pretoria, Pretoria 0028, South Africa

To overcome the disadvantages of the cylindrical holes in the film-cooling, complex geometries of the fan-shaped diffused holes are employed in the cascade investigations. The present experiment employs a new design of diffused hole for film-cooling which is formed by diffusing a cylindrical hole smoothly only in the forward direction. The aerothermal performance in a linear vane cascade are compared between an array of simple cylindrical holes and an array of diffused cylindrical holes by employing them in the cascade upstream-endwall. The objectives are to increase the aerothermal performance of the cylindrical holes in the gas-turbine passage film-cooling. The measurements of temperatures, velocity, flow angle, and total-pressure losses are obtained at the inlet Reynolds number of 2.0E+05, and coolant-to-mainstream density ratio of 1.0 and temperature ratios between 0.94 and 1.0. Four inlet blowing ratios of the film-cooling flow are tested. The results show less coolant migration into the boundary layer and passage vortex for the diffused holes than for the cylindrical holes. The passage vortex becomes weaker and overall total-pressure losses at the passage exit are lower for the diffused holes. The local and average adiabatic film-cooling effectiveness along the endwall are always higher for the diffused holes.

Keywords: passage-vortex; coolant mass-flux; total pressure-loss; film-cooling effectiveness; film-cooling distributions.

Nomenclature

C, C_{ax}	=	Vane profile actual and axial chord
$C_{p,w}$, $C_{Pt,loss}$	=	Endwall pressure coefficient and total-pressure loss coefficient
D, L	=	Film-cooling hole diameter and length

[1] PhD student, Mechanical and Aeronautical Engineering Department.
[2] Senior Lecturer, Mechanical and Aeronautical Engineering Department.
* Corresponding author. Present address: Prince Mohammad Bin Fahd University, Saudi Arabia, gmahmood@pmu.edu.sa.

LE, TE	=	Vane leading-edge and trailing-edge
M, (MFR)	=	Inlet blowing ratio (BR) and mass fraction ratio of film-cooling (M_c/M_a)
M_a, M_c	=	Mass flow rate in one passage: mainstream and film-cooling flow
P, S	=	Two-dimensional vane pitch and span
PS, SS	=	Passage pressure-side and suction-side
$P_{s,r}$, $P_{t,r}$	=	Reference pressure: static and total
$P_{t,b}$, $P_{t,f}$	=	Total pressure in plenum-box and test plane
P_{wall}	=	Endwall static-pressure
Re	=	Inlet Reynolds number to cascade, $(\rho_r UC/\mu)$
$T_{c,b}$	=	Air temperature (K) in coolant plenum
T_f, T_r	=	Air-flow temperature (K) in test planes and reference plane
T_w	=	Local endwall temperature (K)
T_{wall}, T_{pixel}	=	Surface temperature (°C) from thermocouple and image-pixel
U	=	Freestream velocity along X_G at reference
(X, Y, Z)	=	Local Cartesian coordinates
(X_G, Y_G, Z_G)	=	Global Cartesian coordinates
ΔYaw	=	Yaw-angle deviation (deg)
(u, w)	=	Local velocity components: along X_G and Z_G
μ, ρ_r	=	Air density and viscosity in reference plane
$\rho_{c,b}$	=	Air density in coolant plenum
η	=	Adiabatic local film-cooling effectiveness
$\eta_{pitch-av}$, η_{av}	=	Average adiabatic film-cooling effectiveness: pitchwise and global
γ, γ_{ms}, $\gamma_{ms,av}$	=	Yaw-angle in deg: local, mid-span, and average at mid-span

I.   Introduction

Different geometries and arrangements of the film-cooling hole are investigated in the cascade passage for the full-coverage endwall film-cooling in the gas turbine vane and blade passages. Cylindrical hole and fan-shaped hole, which is the common geometric variation of the cylindrical hole, are the typical geometries of the film-cooling holes. The cooling holes are generally arranged in rows in the endwall upstream and inside passage of the cascade. The upstream-endwall holes are

important as they provide film-cooling coverage on the endwall near the vane and blade leading edge regions as well as in the region upstream of the three-dimensional flow separations on the endwall. The geometry and arrangement of the holes are also vital for the control of endwall secondary flows and aerodynamic losses across the cascade passage. The present experimental investigation initially employs cylindrical holes in the pitchwise rows in the upstream-endwall of a vane cascade. Diffused cylindrical holes later replace the cylindrical holes. The diffused hole is a simple geometric modification of the cylindrical hole to smoothly diffuse the coolant ejection at a mild angle. The objectives are to compare the aerothermal performance of the film-cooling flow between the two types of holes in a vane cascade: simple cylindrical holes and diffused cylindrical holes. The compatibility of the diffused hole performance with the fan-shaped hole performance is also examined.

The experimental and numerical results of endwall heat transfer and film-cooling effectiveness in Refs. [1-3] are obtained with the cylindrical film-cooling holes either in a single or two-row arrangements in the upstream endwall. The results in Refs. [1-3] are affected as the film-cooling flow interacts with the endwall region flows and migrates away from the endwall and pressure side of the cascade passage. Wang et al. [4] employs two rows of cylindrical holes at the upstream-endwall as well as at the downstream of mid-passage locations in the cascade endwall to show the upstream holes are the most effective in the film-cooling coverage and higher adiabatic effectiveness. Li et al. [5, 6] also investigate with the cylindrical holes in the upstream and inside endwall of a vane cascade. However, the upstream holes in Refs. [5, 6] result in only desirable high and uniform adiabatic film-cooling effectiveness at the high coolant flow rate when the passage vortex and cross-pitch pressure gradient are affected significantly. The investigations of Refs. [7-11] suggest that the film-cooling effectiveness on the cascade endwall provided by the upstream cylindrical holes can be improved significantly when aided by the upstream slot film-cooling flow. The aerodynamic performance of the cascade in Refs. [7-11], however, suffers as the combination of holes and slots for the endwall film-cooling is employed. In contrast, when the endwall film-cooling of the leading-edge cylindrical holes in Refs. [12, 13] is aided by the leading-edge or upstream slot film-cooling flow to enhance the cooling effectiveness, the leading-edge horseshoe vortex and passage vortex are reduced significantly. The trenched cylindrical holes in the upstream endwall employed by Sundaram and Thole [14] also improve the film-cooling coverage by keeping the coolant stream adjacent to the endwall. The non-uniform mainstream flow imposed by Barigozzi et al. [15] and Yang et al. [16] on the endwall film-cooling flow supplied from cylindrical holes in the upstream-endwall of cascade causes significant losses in the aerodynamic performance and coolant coverage on the passage pressure-side.

Kunze et al. [17] show the film-cooling from the fan-shaped holes in endwall at the cascade inlet negatively influences the aerodynamic losses and film-cooling effectiveness distributions at the high loading condition on the vane. The endwall film-cooling effectiveness for the fan-shaped holes in Zhang et al. [18] remains largely the same with and without filleted vane. Barigozzi et al. [19] measure the effects of exit-area of the fan-shaped holes to find the small exit-area reduces the

aerodynamic losses and the large exit-area improves the film-cooling effectiveness. The fan-shaped holes outperform the cylindrical holes in the cascade endwall for the adiabatic film-cooling effectiveness in Refs. [20]. The forward expansion angle, lateral expansion angle, and length of the fan-shaped hole of Yang et al. [21] and Seo et al. [22] influence the film cooling effectiveness.

The past investigations with the cylindrical film-cooling holes in the upstream-endwall of the vane cascade provide much higher cooling effectiveness near the suction-side regions of the passage endwall compared to the cooling effectiveness near the leading-edge and pressure-side regions. Also, the effectiveness distributions depend on the upstream locations of the cylindrical holes relative to the vane leading edge. The fan-shaped holes are employed to provide better distributions of the film-cooling flow and adiabatic effectiveness on the endwall than the cylindrical holes. However, the aerodynamic losses across the cascade passage increase with the fan-shaped holes because of the coolant mixing with the boundary layer flow. Also, the complex geometry of the fan-shaped hole introduces some flow losses inside the holes increasing the cascade overall aerodynamic losses. The coolant coverage of endwall along the axial direction is somewhat restricted because of the lateral diffusion of the fan-shaped holes. The jet-momentum of coolant flow at the hole exit reduces along the hole axis but increases along the endwall for the forward diffusion of cylindrical hole. Consequently, the coolant lift-up from the endwall and the pressure losses are expected to reduce and the film-cooling effectiveness is expected to increase for the diffused cylindrical hole. The present diffused cylindrical holes are designed by curving the cylindrical holes in the forward diffusion form smoothly. The modified shape and the base cylindrical shape are experimented for the uniform distributions of the film-cooling flow along the endwall along with the aerodynamic losses inside the vane cascade. Both the cylindrical and diffused holes are employed in the upstream-endwall near the cascade inlet. Measurements of the near endwall flow-field and endwall adiabatic temperatures are obtained along the cascade passage with both types of holes separately. All the tests are conducted at a constant Reynolds number of 2.0E+05 and a constant coolant-to-mainstream flow density ratio of 1.0 as the inlet blowing ratio of the film-cooling flow varies between 1.0 and 2.2.

II.   Experimental Setup and Methods

A. Wind tunnel and vane cascade

Figure 1(a) shows the atmospheric wind tunnel that houses the cascade test section with seven two-dimensional vanes. The vane profiles are numbered 1 to 7 in the cascade. The profiles are generated from the hub-side profile of the three-dimensional nozzle guide vane of the GE-E^3 gas turbine [23]. The linear extrusion of the profile is then used to create the vanes in the experimental cascade. The polycarbonate skin of the vane is laminated for the extra-smooth surface finish. The cross-section of the entire wind tunnel is rectangular. The walls are constructed of particle-woods and acrylic plastics. The

clearance gaps between the side-walls and side vanes (vane-1 and vane-7 in Fig. 1(a)) are used to maintain the flow periodicity in the vane passages. Table 1 provides details of the cascade geometry. The suctions of two duct-fans connected in series on the flow exit-side generate an air-speed of $U = 10.0$ m/s at the cascade inlet. A two-dimensional contraction with the honeycomb screens at the wind tunnel entry accelerates the atmospheric air smoothly. Turbulence in the incoming flow is generated by employing a passive grid at $6.5C_{ax}$ upstream of the cascade inlet as shown in Fig. 1(a). The streamwise (freestream) turbulent intensity is measured with a constant temperature anemometer. The reference properties of the flow for the measurements are obtained in a transverse-plane (reference plane) located $2.5C_{ax}$ upstream of the cascade and are provided in Table 2. The Reynolds number, Re in the table is estimated based on the reference velocity, U and vane profile chord length, C. The properties in Table 2 are the averages of the scanned local values in the reference plane. The freestream velocity, turbulence intensity, and temperature (T_r) in the table are reported above the velocity boundary layer of the bottom endwall. The temperature ratio, $T_{c,b}/T_r$ in Table 2 is about 0.94 for measurements of the flow temperature and film-cooling effectiveness and is about 1.0 for all the other measurements. An exchangeable rectangular plate identified as the "Film cooling plate" in Fig. 1(a) is located in the bottom endwall just upstream of the cascade inlet. The cylindrical film-cooling holes are machined in the plate. A similar plate with the formed diffused cylindrical holes (discussed later in Section II(B)) replaces the existing plate for the measurements with the diffused holes. The test facility is described in detail in Ref. [24] with all the geometric parameters and materials. The flow condition is considered incompressible because of the small pressure drop across the cascade. Cut-out slots on the top endwall allow for the insertion of probes for the velocity, temperature, and pressure measurements in the cascade. A pair of overlapping tapes masks a slot to minimize the air leaks when a probe is traversed for measurements. The yellow-highlighted passages of Fig. 1(a) between vanes-3 and 4 and between vanes-4 and 5 are instrumented for the measurements. Figure 1(b) shows the measurement locations, arrangements, and coordinate systems with Y_G or $Y = 0$ located on the bottom endwall. The locations of the four flow-measurement planes identified as the Plane-1 to Plane-4 in Fig. 1(b) are referenced from the vane leading-edge. The Plane-1 to Plane-3 are located inside the passage and upstream of the passage-throat between vane-3 and vane-4. The transverse pitchwise Plane-4 is located slightly downstream of the vane trailing-edge. The Planes-1 and 2 are oriented perpendicular to the local vane surface while the Planes-3 and 4 are perpendicular to the direction X_G. A window in the top endwall is used to access for the camera view for the thermal imaging of the bottom surface which is film-cooled. All the measurement locations and coordinates in Fig. 1(b) are employed in the passage between vane-3 and vane-4.

The coolant-flow to the holes in the film-cooling plate is supplied by employing a secondary flow circuit. The details of the flow circuit including the flow rate and temperature measurements are provided in Refs. [24, 25] and hence, are not repeated here. A separate blower forces the coolant air through a metered pipe section in the circuit. The air flows through a

chiller unit of a vapour-compression system that controls the air temperature. The cooled flow is then fed into the film-cooling holes through a large plenum located underneath the bottom endwall of the cascade. The plenum walls and bottom endwall in the measurement passages are thermally insulated. The conduction flux through the bottom endwall due to the temperature difference between the mainstream and plenum air is thus minimized during the tests for the film-cooling effectiveness. The inlet blowing ratio, M of the overall film-cooling flow is computed from Eq. (1). The speed of the small amount of coolant flow in the large plenum is negligible to approximate the measured static-pressure at the plenum wall to be the total-pressure, $P_{t,b}$. Table 3 provides the mass fraction ratio (M_c/M_a) of the overall coolant flow to the passage flow in the test passage between vane-3 and vane-4. The mass flow rate in the passage, M_a is estimated from the passage inlet area ($P*S$) and reference velocity (U).

$$M = \left(\frac{P_{t,b} - P_{s,r}}{P_{t,r} - P_{s,r}} \right)^{\frac{1}{2}} \qquad (1)$$

B. Film-cooling holes

Figure 2 provides the geometries, positions, and arrangements of the film-cooling holes in the film-cooling plate relative to the locations of vanes-3, 4 and 5. Two types of holes are employed in the film cooling plate separately: simple cylindrical holes in the "Case-a" arrangement and diffused cylindrical holes in the "Case-b" arrangement. As shown in Fig. 2, some of the cylindrical holes in Case-a are placed in one pitchwise-row between the vanes and the others in two pitchwise-rows in the leading-edge region. All the diffused cylindrical holes in Case-b are placed in a single pitchwise-row. Note, the pitchwise spacing between the holes is different for the two Cases. As shown in Fig. 2, the number of cylindrical holes is 27 in one pitch between the vanes with the pitchwise spacing between the holes varying from 12.2 mm to 13.7 mm. The number of diffused holes in Case-b is 22 in one pitch between the vanes with the constant pitchwise spacing of 13 mm between the holes. The cylindrical holes of diameter 5.0 mm are oriented at 30° relative to endwall surface with the ratio, $L/D = 8$. The compound or yaw angle relative to the main-flow direction, X_G is 0° for both the cylindrical and diffused holes. Most of the past cascade investigations reported in the literatures employs the cylindrical holes at angles between 25° and 35° with the 0° compound angle in the upstream-endwall. The cylindrical holes in the present investigation are drilled in an acrylic plate used as the film-cooling plate in Fig. 1(a).

The diffused cylindrical hole is created by diffusing the cylindrical hole in the forward direction only in the meridional plane of cross-section as indicated in Fig. 2. The inlet part of the hole has the diameter of 5.0 mm and is angled at 30° relative to endwall. As shown in the figure for Case-b hole-geometry, the front-line on the cylinder surface in the meridional cross-section starts to diffuse or curve-out at 17.3 mm from the inlet along a circular arc toward the downstream or front side. The

rear-line in the meridional cross-section starts to curve-in at 26 mm along a circular arc toward the cylinder front side. The cross-sections of the diffused hole at every point on the meridional-axis, i.e., cross-sections perpendicular to axis, remain circular to generate a diffusion primarily in the forward direction along X_G. The exit of the diffused hole is then angled at 7° at the front side and at 20° at the rear side relative to the endwall in the meridional cross-section as shown. The ratio of L/D = 8.9 for the diffused hole is then based on the length of the axis line (broken line), L = 44.6 mm. The planar area of the hole-exit on the endwall is 646 mm² for the diffused hole compared to 157 mm² for the cylindrical hole. The geometry of diffusion is decided based on two reasons: (i) to avoid a flow separation of coolant inside the hole, and (ii) to eject the coolant smoothly to minimize the penetration into the boundary layer and transport the coolant adjacent to the endwall a long distance by its momentum. The abrupt change of flow angle by the diffusion of the fan-shaped hole always introduces some flow separations [26, 27] resulting in the additional pressure losses in the cascade. The present test setup does not allow any flow measurements inside the film-cooling holes. The work of Gritcsh et al. [28] suggests any ratio of $7.5 < L/D < 11.5$ is optimum for the high film-cooling effectiveness. The metering section of the present diffused hole, which is the constant diameter inlet section, has the length-to-diameter ratio of 3.5 based on the Refs. [26-30] to fully develop the coolant flow upstream of the diffusion. The forward diffusion angle of the present hole is 23° based on the inlet angle (30°) and front exit angle (7°). This value of 23° is much larger than the common diffusion angles between 7° and 15° employed by many recent investigations, e.g., Refs. [17-22, 26-31]. However, the total diffusion angle at exit is 13° based on the rear exit angle of 20° and front exit angle of 7° in the meridional cross-section. Only one geometry of the diffused hole shown in Fig. 2 is tested. The variations of the diffused hole-geometry can be subject of future experiments. The present diffused holes are printed in a commercial three-dimensional printer with the standard ABS plastic filament. The porosity in the printing is set at 0%. The printed film-cooling plate is treated chemically for a smooth surface finish inside the diffused holes.

The present cylindrical holes and diffused holes are also tested for the discharge coefficients in an experimental facility very similar to the one in Bell et al. [31]. The two types of holes are employed separately in a flat endwall of the low speed wind tunnel at a low mainstream turbulence (~ 1%). The coolant-to-main flow temperature ratio and density ratio are both 1.0 for the tests. Figure 3 presents the results of the measured discharge coefficients as the local blowing ratio varies for both the cylindrical hole and diffused cylindrical hole. The local blowing ratio is defined as the ratio of the coolant mass-flux in a film-cooling hole to the mass-flux in the tunnel mainstream flow [31]. The discharge coefficient in Fig. 3 increases with the blowing ratio. The distribution is similar to the results in Aghasi et al. [30]. However, the discharge coefficients are always higher for the diffused hole than for the cylindrical hole. The flow resistance is thus less in the diffused holes than in the cylindrical holes.

C. Measurement technique

The reference properties in the Table 2 are measured with a pitot-static pressure probe and hot-wire probe inserted through a cut-out slot in the top endwall at the location of the reference plane (refer to Fig. 1(a)). The measured streamwise velocity is presented in Fig. 4(a) as the ratio of X_G-velocity component to freestream velocity, u/U in the reference plane. The boundary layer thickness reaches to $Y/S \approx 0.10$ where $u/U \approx 0.99$. The flow-field in the test planes of Fig. 1(b) is measured with a commercial five-hole pressure probe of tip diameter 1.6 mm also inserted through the cut-out slots in the top endwall. The same thermal probe as in the measurements of Shote et al. [32] is employed to measure the temperature field in the test planes. The probes are traversed along the reference and test planes employing a two-axis motorized traverse. The spatial resolutions of traverse movement are 2.0 mm near the walls and 5.0 mm away from the walls. The number of flow-measurement points varies between 1200 and 1500 depending on the test plane location. Each port of a traversing pressure probe is connected to one differential pressure transducer. The five-hole pressure probe is connected to five pressure transducers. Further details of the flow measurement setup are provided in Arnachellan [24]. The analog data are scanned and digitized at the sampling rate of 100 Hz over 2 sec for the pressure, 60 Hz over 2 sec for the temperature, and 5 kHz over 10 sec (hot-wire probe) for the turbulence intensity through the National Instruments^{TM} data-acquisition systems. One single Labview^{TM} computer program records the data and controls the traverse motion. The voltage data from the data-acquisition systems are time-averaged and then converted into the units of flow properties after applying the appropriate calibration curves. Arnachellan [24] provides the calibration curves and the corrections for the probe dimensions for the five-hole pressure probe measurements.

The endwall temperature distributions for estimating the film-cooling effectiveness are obtained from the infra-red thermal image of the endwall surface in the cascade measurement area between the vane-3 and vane-4. The thermal image of the cooled bottom-endwall is captured with a commercial infra-red video camera having an image resolution of 320 pixels by 256 pixels with a 16-bit pixel depth. The model of FLIR infrared camera is Ax5-Series. The camera views the bottom-endwall through a Zn-Se window installed in the top-endwall (refer to Fig. 1(b)) and captures the images at a frame rate of 60 Hz and at an emissivity setting of 0.96. The endwall surface is covered with a thin layer of copper sheet which is painted flat-black on the flow side for the maximum emissivity and minimum reflections. The Zn-Se window passes the infra-red wavelengths between 5 μm and 98 μm. Four viewing windows in the top endwall are used to cover the image of endwall between the vane-3 and vane-4 of Fig. 1. The digitized image-frames from the captured video are time-averaged over 20 sec at each window location. The pixel values in the thermal image are converted into the temperature (°C) using an image-grabbing computer program and the internal calibrations proprietary to the camera manufacturer. The images from the four windows are then patched to produce the thermal image of the entire endwall surface. The pixel temperatures of the time-averaged thermal

image are converted into the true surface temperatures on the endwall by employing the in-situ calibration technic described by Sargent et al. [33]. Forty-five calibrated thermocouple tips are placed along the endwall at known locations for the in-situ calibrations of the pixel temperatures in the thermal images. The thermocouple tips are inserted through drilled holes in the bottom endwall to place them adjacent to the copper sheet. The thermocouple wires are fixed in the hole by gluing to the hole-wall. The gaps between the thermocouple wires and hole-wall are filled in with a thermal paste. To avoid any gap between the copper sheet and thermocouple tip and ascertain the tip remains attached to the copper, the tip is also covered with the thermal paste. Because of the high thermal conductivity of the thermal paste and copper sheet, the temperature read by the thermocouple is assumed to be same as the surface temperature on the flow side of the copper sheet. Any conduction loss through the endwall during the film-cooling measurements is thus accounted for in the temperature readings by the thermocouples. No temperature corrections are applied to the thermocouple readings due to the conduction loss.

Figure 4(b) shows the results of a sample in-situ calibration of the pixel temperatures of the thermal image at the surface thermocouple locations. The calibration data for the pixel temperatures between 11 °C and 18 °C are obtained in a window location during the adiabatic film-cooling effectiveness test at $M = 1.8$ for the Case-b. The horizontal axis, T_{pixel} (°C) in the plot of Fig. 4 represents the pixel temperatures at the thermocouple-tip locations and the vertical axis, T_{wall} (°C) represents the corresponding thermocouple temperatures or the endwall-surface temperatures at the thermocouple locations after accounting for the conduction loss in the endwall. A thermal image for a viewing-window position contains the locations of at least 10 thermocouple tips, i.e., 10 calibration data points. The least square-fit of the linear regression analysis through the calibration data points is applied for the curve-fit shown in Fig. 4. The equation of the curve-fit determines the relationship between a pixel-temperature and an actual wall-temperature at the image-pixel location during an actual test condition [33]. The correlation of coefficient for the curve-fit is 0.97 or higher for an in-situ calibration of the thermal image. The local adiabatic film-cooling effectiveness, η on the endwall is estimated from Eq. (2). The local wall temperature, T_w in the equation is obtained after applying the in-situ calibration (curve-fit equation) of the pixel temperature to the thermal image.

$$\eta = \frac{(T_r - T_w)}{(T_r - T_{c,b})} \tag{2}$$

Measurements of the wall-static pressure are obtained at the pressure-tap holes located along the endwall. The pressure-tap holes are distributed evenly along the pitchwise and streamwise directions in the endwall between vane-3 and vane-4 [24] and connected to a single pressure transducer via a manual scanner [24]. The top endwall opposite to the film-cooled endwall of the passage is instrumented with the pressure-taps. The signals from each tap are recorded at 100 Hz for 2 sec for the time-averaging and then converted into the pressure unit after applying the appropriate calibration. There are no upstream film-cooling holes in the top endwall. The endwall-pressure distribution provides the pitchwise pressure differences in the passage

to indicate the locations of strong cross-pitch flow near the endwall which is a determinant of the film-cooling flow distributions.

D. Uncertainty estimates

The errors in the measured quantity and calculated data are estimated based on the 95% confidence interval as described in Refs. [34, 35]. The uncertainties in velocity and pressure (gage) are 1.6% and 3.6%, respectively. The zero-offset voltages of the pressure transducers are accounted in the calibrations to reduce the bias-errors. The wall-pressure coefficient and total-pressure loss coefficient have the maximum uncertainty of 5.7% and 8.2%, respectively. The yaw-angles near the wall regions have uncertainties of 5% and less. The maximum uncertainty in the film-cooling flow rate is 0.7% and in the inlet blowing ratio is 1.4%. The maximum uncertainty in the thermocouple temperature is 4.0% and non-dimensional temperature is 6.9%. The thermal image data then have the maximum uncertainties of 6.1% in the temperature and 10% in the adiabatic effectiveness.

III.   Results and Discussions

The results presented here are measured in the passage between vane-3 and vane-4 as indicated earlier in Section II(A). The reference properties used to normalize the measured data are already listed in Table 2. All the measurements are obtained as the velocity, temperature, and pressure reach at the quasi-steady state when the changes are within ± 0.1 °C for temperature and ± 2 Pa for pressure over a 10 minute period. The flow condition in the cascade passages is periodic as shown by Mahmood and Arnachellan [25] and Shote et al. [32] in the same cascade for various test conditions. The Reynolds number based on the inlet velocity to the cascade passages is about 2.0E+05. Although all the test conditions do not replicate the actual engine conditions, the basic flow features, e.g., the endwall boundary layers, LE horseshoe-vortex, endwall passage-vortex legs, pitchwise pressure gradient, and interactions between the endwall film-cooling flow and boundary layer are present both in the cascade passages and gas turbine passages. The results on and near the endwall region in the present investigation are thus relevant to the gas turbine passages. The passive turbulence grid of the wind tunnel provides a low freestream turbulence of 3% at the reference plane and cannot control the turbulence level. The effects of freestream turbulence are not a part of the present investigation. The flow-field in the present cascade without the film-cooling (baseline case) is not discussed for it has been reported by Ref. [25].

A. Endwall pressure coefficient, $C_{p,w}$

The measured static-pressures, P_{wall} along the endwall are normalized in Eq. (3) and presented as the distribution of $C_{p,w}$ contours in Fig. 5. The vane locations, pressure-side (PS), and suction-side (SS) of the passage are also identified in the figure.

The labels on the contour lines represent the values of $C_{p,w}$. The $C_{p,w}$ values increase along the passage from the LE to TE and from the PS to SS along a pitch-line as the P_{wall} decreases for the flow accelerations. Figure 5 shows the $C_{p,w}$ values increase significantly from the PS to SS pitchwise in the upstream half of the passage in $X_G/C_{ax} < 0.5$ compared to the downstream half in $X_G/C_{ax} > 0.5$. The locations of $X_G/C_{ax} < 0.5$ are also the upstream of the three-dimensional flow separation line as shown in Refs. [10, 36] for the similar vane passages. The significantly high pitchwise pressure-gradients in $X_G/C_{ax} < 0.5$ will cause the near endwall streamlines as well as the film-cooling flow to turn away significantly from the PS toward the SS [5, 10, 36]. The streamlines near endwall are more uniform in the downstream region in $X_G/C_{ax} > 0.5$.

$$C_{p,w} = \frac{\left(P_{s,r} - P_{wall}\right)}{\left(P_{t,r} - P_{s,r}\right)} \tag{3}$$

B. Non-dimensional temperature, θ

The temperature field of flow near the endwall indicates the coolant concentration along endwall and the depth of penetration of coolant flow into the mixing-layer. The film-cooling flow penetrating into the mixing-layer high above the endwall mixes with the hot combustion gas and loses the ability to cool and cover the endwall from the hot gas effectively. The high concentration or distribution of the coolant mass adjacent to the endwall, which is indicated by the low temperature distributions of flow, is thus desirable. The measured local air-temperatures, T_f near the endwall in Planes-1, 2, and 3 are normalized in Eq. (4) and presented in Figs. 6 to 11 as the distributions of θ contours for cylindrical (Case-a) and diffused (Case-b) holes. Only one legend of the contour distributions is used for both Cases-(a, b) and shown at the bottom of the plots in each figure. The relative locations between the upstream holes and test planes inside the passage are indicated by the isometric three-dimensional view of the vane passage. According to Eq. (4), the lower the T_f, the lower the θ for the controlled coolant-temperature, $T_{c,b}$ remains approximately constant. The low values of θ distributions indicate the high coolant concentration desirable adjacent to the endwall. The low θ distributions away from the endwall then indicate the coolant mixing with the mixing-layer and the loss of film-cooling coverage on endwall. The distributions of θ in each test plane in Figs. 6 to 11 are shown for the two blowing ratios, e.g., $M = 1.8$ and 2.2.

$$\theta = \frac{\left(T_f - T_{c,b}\right)}{\left(T_r - T_{c,b}\right)} \tag{4}$$

The pressure-side of the passage (PS) in the Plane-1 of Figs. 6 and 7 is located on the right-hand side. The contour values of $\theta < 0.9$ are seen away from the PS for both Case-a and Case-b as the film-cooling flow is turned and swept toward the suction-side by the strong cross-pitch flow [36] and pitchwise pressure gradient (refer to Fig. 5). As the blowing ratio is increased from $M = 1.8$ to 2.2, the lower values of θ move closer to the PS in Fig. 7 than in Fig. 6 for the higher momentum

of the coolant jet at $M = 2.2$ transports more coolant near the PS. The film-cooling flow thus covers more endwall region when the blowing ratio is increased to $M = 2.2$. When the two Cases are compared at a blowing ratio either in Fig. 6 or in Fig. 7, the lower values of $\theta \leq 0.8$ are distributed higher above the endwall ($Y/S > 0.02$) for Case-a than for Case-b indicating more losses of coolant into the boundary layer for the cylindrical holes (Case-a). The momentum of the film-cooling jet adjacent to the endwall is higher for the Case-b causing the less penetration of coolant into the boundary layer above the endwall. The values of θ at a near wall location $Y/S = 0.016$ are also plotted along Z/P in Figs. 6 and 7 to provide better quantitative comparisons between Case-a and Case-b. This Y/S location can be considered as the bottom part of the incoming boundary layer to the cascade. Away from the pressure-side (PS) as Z/P decreases at $Y/S = 0.016$, the θ values for Case-b are higher than for Case-a as the coolant-jet turns less toward the suction-side and it is present in less amount away from the $Z/P = 0$ position for the Case-b (diffused holes). The higher momentum of the coolant jet for the Case-b is responsible for less turning of the coolant. The θ values for the Case-b in the line-plots are smaller in Fig. 7 than in Fig. 6 as the amount of coolant increases for $M = 2.2$. The film-cooling coverage of the endwall as a consequence is expected to be better for Case-b than for Case-a.

Figures 8 and 9 compare the θ distributions in the Plane-2 between Case-a (cylindrical holes) and Case-b (diffused holes). The suction-side of the passage (SS) is located on the left-hand side in the contour plots. The low values of $\theta < 0.9$ are located along the entire endwall in the plane with lower values of $\theta \leq 0.8$ concentrated near the SS corner. However, the θ values are smaller near the SS for Case-a than for Case-b in the Plane-2 at a blowing ratio because of the higher amount of coolant flow from the double row of cylindrical holes near the LE. The position of suction side-leg vortex for the Case-a in the Plane-2 may also cause lifting and concentration of the lower θ values near the SS corner. Note, the low values of $\theta \leq 0.8$ is always closer to the endwall for Case-b than for Case-a at a blowing ratio. As the blowing ratio is increased from $M = 1.8$ to 2.2, the low values of θ distributions reach higher above the endwall in Fig. 9 than in Fig. 8. The higher momentum of the film-cooling jet adjacent to endwall for the Case-b in Plane-2 also causes the less turning of coolant toward the SS as well as the less penetration of coolant into the boundary layer. The line-plots on the right-hand side in Figs. 8 and 9 compare the θ values near wall at $Y/S = 0.016$ along Z/P. For $M = 1.8$ in Fig. 8, the higher amount of coolant for Case-b causes the lower values of θ near the suction-side (SS) compared to those for Case-a in the line-plot. As the blowing ratio increases to $M = 2.2$ in Fig. 9, the amount of coolant flow also increases from the double row of cylindrical holes near the leading-edge in the Case-a resulting in the comparable θ values near the SS between Case-a and Case-b in the line-plot. The endwall near the suction-side of the leading-edge region is thus better covered by the film-cooling at higher M irrespective of the cooling-hole geometry.

The distributions of θ in Figs. 10 and 11 are compared between Case-a and Case-b in the Plane-3 that covers the entire pitch in the passage. The pressure-side (PS) and suction-side (SS) are located on the right-hand and left-hand side,

respectively, of the plots. In the Plane-3 also, the low values of $\theta \leq 0.8$ are distributed closer to the endwall for Case-b than for Case-a at a blowing ratio. Similar to the Plnae-2, there are also more concentrations of lower values of $\theta \leq 0.7$ in the Plane-3 near the SS for Case-a than for Case-b because of: (i) the more amount of coolant mass from the LE cylindrical holes, (ii) the more turning and sweeping of the coolant streams delivered from the cylindrical holes away from the LE, and (iii) the lifting and entrapment of the lower θ values by the suction side-leg vortex in the Case-a. Migration of the coolant jet from the cylindrical film-cooling holes in the leading-edge endwall to the high spanwise locations on vane suction-surface is also evidenced in Refs. [2, 3, 7]. When the blowing ratio, M is 2.2, the distributions of $\theta \leq 0.9$ spread higher above the endwall as well as pitchwise for both Case-a and Case-b as the coolant spreads everywhere with high momentums. The coolant migration and mixing with the boundary layer cause the high values of θ and mixing losses near endwall that increase with M and are shown later by the results of total pressure losses. As in the other planes, the higher momentum of the coolant jet along and adjacent to the endwall for the Case-b is responsible for the low values of θ distributions in the Plane-3 in Figs. 10 and 11. The line-plots on the right-hand side in Figs. 10 and 11 compare the θ values near wall at $Y/S = 0.016$ along the pitch line (Z/P). The θ values near the pressure-side (PS) in the line-plots are smaller for Case-a than for Case-b as the amount of coolant from the double row of cylindrical holes is higher for the Case-a. The Plane-3 is located downstream of the passage vortex region. The amount and momentum of the coolant jet from the cooling-holes near the leading-edge region are primarily responsible to cover the endwall region near the pressure-side downstream of the passage vortex.

C. Streamline velocity ratio (u*) and Yaw-angle deviation (ΔYaw)

Figures 12(a, b) and Figures 13(a, b) present the distributions of streamline velocity ratio, u^* in the Plane-3 for Case-a and Case-b of the film-cooling arrangement. Equation (5) defines the u^* where the numerator is the local streamline velocity based on the mid-span flow yaw-angle, γ_{ms} and the denominator is the streamline velocity at the mid-span (ms), i.e., at $Y/S = 0.5$. The local mid-span components (u_{ms}, w_{ms}, γ_{ms}) in the equation are obtained at the same Z/P location as the Z/P location of (u, w). The value of $u^* \approx 0.99$ defines the edge of velocity boundary layer. Note, the boundary layer thickness at the cascade passage inlet is $Y/S = 0.1$ as indicated in Table 2. The data of Figs. 12(a, b) and Figs. 13(a, b) illustrate the local distributions of coolant and interactions between the coolant and boundary layer in the endwall region. Only one color legend of the contour distributions of u^* is used for both the Cases in the figures.

$$u^* = \frac{[u \cdot Cos(\gamma_{ms}) - w \cdot Sin(\gamma_{ms})]}{[u_{ms} \cdot Cos(\gamma_{ms}) - w_{ms} \cdot Sin(\gamma_{ms})]} \tag{5}$$

The values of $u^* \geq 1.0$ along and above the endwall in Fig. 12 and Fig. 13 are the direct evidences of coolant streamlines and effects of coolant flow on the boundary layer. The values of $u^* \leq 0.98$ near the SS in the same figures are caused by the

strong secondary flows of the passage vortex. Mahmood et al. [36] show the passage vortex structures are located near suction-side at the mid-passage where the present Plane-3 is located. The pitchwise locations of higher and lower values of $u*$ along endwall are about the same for Case-a and Case-b in Figs. 12(a, b) as well as in Figs. 13(a, b). However, the region of $u* \geq 1.04$ adjacent to the endwall either in Figs. 12(a, b) or Figs. 13(a, b) is slightly larger for Case-a than for Case-b because of the transport of local coolant amount from the LE region cooling holes to the passage PS region. The number of cylindrical film-cooling holes is twice the number of diffused film-cooling holes upstream of the vane LE. The amount of coolant flow from the LE cooling holes is thus larger for the cylindrical holes than for the diffused holes. The $u*$ data near the PS are thus affected differently for Case-a from Case-b. For the same reason of larger amount of coolant flow from the LE cooling holes for the cylindrical hole case (Case-a), the low-value region of $u* \leq 0.98$ is slightly larger for Case-b than for Case-a. Also, the region of $1.02 \geq u* \geq 1.04$ increases near the PS and the region of $u* \leq 0.98$ reduces near the SS when the M increases from Fig. 12 to Fig. 13. The results of $u*$ in Figs. 12 and 13 concur with the θ distributions in the Plane-3 as the more coolant flows from the leading-edge holes, more coolant is entrapped by the passage vortex, and more coolant migrates into the mixing-layer for Case-a than for Case-b. The migration of coolant into the mixing-layer increases the secondary flow losses and reduces the adiabatic effectiveness which are presented later. More differences in $u*$ between the cylindrical and diffused holes are present very close to the endwall which cannot be measured due to the probe dimensions. The line-plots of $u*$ at the bottom of Figs. 12 and 13 show the data along the pitchwise Z/P at the near-endwall location of $Y/S = 0.023$. The differences in $u*$ between Case-a (cylindrical hole) and Case-b (diffused hole) near the suction side $Z/P = 0$ are clearly apparent because of the passage vortex.

Figures 12(c, d) and Figs. 13 (c, d) compare the yaw-angle deviations, ΔYaw at $M = 1.8$ and $M = 2.2$, respectively, between Case-a and Case-b in the Plane-3. Equation (6) computes the ΔYaw from the measured local flow yaw-angle, γ. The value of $\gamma_{ms,av}$ in the equation for a test case is estimated from the average of local yaw-angles at the mid-span location of $Y/S = 0.5$. The form of Eq. (6) removes the bias-error in the ΔYaw data which is introduced by the orientation angle of five-hole pressure probe. The distributions of ΔYaw complement the data of $u*$. Mahmood and Arnachellan [25] have shown that for the baseline cascade without the film-cooling the ΔYaw values increase closer to the endwall for the velocity boundary layer and pitchwise pressure gradient. The near-endwall distributions of ΔYaw in Figs. 12(c, d) and Figs. 13 (c, d) are the results of coolant flow and interactions between the coolant and boundary layer. The ΔYaw value increases or is high when the local flow turns toward the SS from the axial direction.

$$\Delta Yaw = \gamma - \gamma_{ms,av} \qquad (6)$$

In Figs. 12(c, d) and Figs. 13(c, d), the ΔYaw distributions of higher values near the SS are caused by the migration of coolant flow as illustrated by the results of u^*. Between the film-cooling Cases, the values of ΔYaw near the SS corner at Z/P < 0.15 are slightly smaller for Case-b than for Case-a because the passage vortex moves higher above the endwall for the Case-a. The ΔYaw distributions at other pitchwise locations of either Figs. 12(c, d) or Figs. 13(c, d) change little between Case-a and Case-b. Note, the decrease in ΔYaw values adjacent to endwall at Y/S < 0.05 and Z/P > 0.15 from Fig. 12 to Fig. 13 when the M increases from 1.8 to 2.2 for the corresponding Cases-(a, b) for the presence of more coolant of higher momentum in the boundary layer. The line-plots of ΔYaw at the bottom of Figs. 12 and 13 compare the data between the two cases along the pitchwise Z/P at the near-endwall location of Y/S = 0.023. The ΔYaw values closer to the 0 value are caused by higher momentum of the coolant jet.

D. Total-pressure loss coefficient, $C_{pt,loss}$

The total-pressure losses across the cascade passage provide an estimate of the aerodynamic losses. The distributions of the total-pressure losses in the flow planes also indicate the location, size, and strength of the passage vortex-legs. The local total-pressure losses are high in the passage vortex and boundary layer regions for the strong secondary flows, entrapment of boundary layer fluid, and mixing with film-cooling flow. Equation (7) defines the total-pressure loss coefficient, $C_{pt,loss}$ with the locally measured total-pressure, $P_{t,f}$ in the test planes. The value of $C_{pt,loss}$ increases with the total-pressure loss, $(P_{t,r} - P_{t,f})$. Figures 14 and 15 show the total-pressure loss coefficients, $C_{pt,loss}$ in the Plane-3 at M = 1.8 and M = 2.2, respectively. The distributions of $C_{pt,loss}$ are compared between Case-a and Case-b in the figures. The passage-vortex and coolant streams at the location of Plane-3 migrate near the suction-side (SS) corner as suggested by Refs. [10, 13, 36]. The high values of $C_{pt,loss}$ > 0.7 in the location of Z/P < 0.3 in both Figs. 14 and 15 are caused by the passage-vortex and mixing losses with coolant. With the increase in the blowing ratio from M =1.8 to M = 2.2, the region of $C_{pt,loss}$ > 0.7 reduces for both Case-a and Case-b for two reasons: (i) the coolant stream momentum increases as the M increases and (ii) the size and strength of the passage-vortex core reduce as the M increases. Also, at a blowing ratio either in Fig. 14 or Fig. 15, the region of $C_{pt,loss}$ > 0.8 is smaller for Case-a than for Case-b indicating higher mixing losses between the passage vortex and coolant for the diffused hole film-cooling. The amount of coolant mass-flux is higher for Case-b than for Case-a. The high value contours of $C_{pt,loss} \geq 1.0$ concentrate closer to the SS for Case-a since the passage-vortex core migrates higher above the endwall which was also speculated for Case-a in the results of Figs. 10 and 11.

$$C_{pt,loss} = \frac{\left(P_{t,r} - P_{t,f}\right)}{\left(P_{t,r} - P_{s,r}\right)} \tag{7}$$

Figure 16 compares the total-pressure loss coefficients, $C_{pt,loss}$ between the Case-a and Case-b at $M = 2.2$ in the Plane-4 downstream of the cascade exit. The axial location of the vane trailing-edge (TE) upstream of the plane is identified at $Z/P = 0.2$ in the figure. The high values of $C_{pt,loss} \geq 6.0$ in the vertical region about $Z/P = 0.2$ are caused by the trailing-edge vortex. The high values of $C_{pt,loss}$ in the region approximately between $0.2 < Z/P < 0.4$ and $0.1 < Y/S < 0.3$ are caused by the passage-vortex core. Part of the passage vortex interacts with the TE-vortex and is not clearly distinguishable in the TE-vortex region in Fig. 16. Migration of the passage-vortex high above the endwall and its interactions with the TE-vortex are also reported by the previous studies on the aerodynamic losses in the exit planes. The high values of $C_{pt,loss}$ adjacent to the endwall at $Y/S < 0.1$ in Fig. 16 are caused by the boundary layer and mixing of boundary layer with the film-cooling flow. This mixing-loss region of $C_{pt,loss}$ adjacent to the endwall is apparently slightly smaller pitchwise for Case-b than for Case-a as a result of higher momentum of the coolant jet from the diffused holes. The $C_{pt,loss}$ region in the passage-vortex core is located slightly higher at $Y/S \approx 0.2$ for Case-a compared to $Y/S \approx 0.15$ for Case-b. Also, the $C_{pt,loss}$ region in the passage-vortex core is slightly smaller for Case-b than for Case-a as the passage vortex becomes weaker and smaller. As shown in Refs. [2, 3, 7], the higher mass of coolant streams from the LE double-row of cylindrical holes partially migrates high above the endwall along the suction-side. The LE coolant streams then increase the mixing losses and strength of the passage-vortex to cause the higher $C_{pt,loss}$ in the passage-vortex core region for Case-a in Fig. 16.

Figure 17 compares the mass-averaged total-pressure loss coefficients, $(C_{pt,loss})_{mass-av}$ between Case- a and Case-b in the Plane-4 as the blowing ratio, M varies. Equation (8) computes the $(C_{pt,loss})_{mass-av}$ integrating numerically the total-pressure loss, $(P_{t,r} - P_{t,f})$. The elemental area, dA in the Eq. (8) is determined based on the spatial resolutions between the measured data points. As shown in Fig. 17(a), the value of $(C_{pt,loss})_{mass-av}$ increases from $M = 1.0$ to $M = 2.2$ for both Case-a and Case-b. The change in $(C_{pt,loss})_{mass-av}$ is minor at $M > 1.8$ for Case-a and at $M = 1.4$ for Case-b. The $(C_{pt,loss})_{mass-av}$ distribution in Fig. 17(a) is always smaller for Case-b than for Case-a. The comparisons between the cylindrical holes and diffused holes in Fig. 17(a) are in agreement qualitatively with the comparisons of the overall total-pressure losses between the cylindrical holes and fan-shaped holes in Colban and Thole [20]. The losses are smaller for the fan-shaped holes than the cylindrical holes [20]. The overall kinetic-energy loss distributions with the coolant flow-rate variations in Ref. [19] suggest that the larger diffusion area of the fan-shaped hole provides higher losses than the cylindrical hole. The local kinetic-energy loss in the exit plane of Refs. [19, 22] is higher in the passage vortex region and in the endwall region where the coolant mixes with the endwall boundary layer. Using an analogy between the total-pressure losses and kinetic-energy losses, the present Case-b of diffused holes is thus expected to cause less kinetic-energy losses compared to the Case-a of cylindrical holes.

$$\left(C_{pt,loss}\right)_{mass-av} = \frac{1}{M_a} \iint \left[\frac{P_{t,r} - P_{t,f}}{P_{t,r} - P_{s,r}}\right]\left(\rho_r u\right)dA \qquad (8)$$

The values of $(C_{pt,loss})_{mass-av}$ are divided by the coolant mass fraction ratio (MFR) to present them in Fig. 17(b). The values of MFR for the cylindrical and diffused holes at the different blowing ratios are listed in Table 3. The ratio, $(C_{pt,loss})_{mass-av}$/(MFR) is important as it estimates the aerodynamic loss generated across the cascade passage per unit of the coolant mass fraction. The low value of $(C_{pt,loss})_{mass-av}$/(MFR) at a high blowing ratio, M indicates the overall pressure loss, $(P_{t,r} - P_{t,f})$ increases little compared to the increase in the coolant mass-flux and is ideal for the cascade aerodynamic-performance. The ratio, $(C_{pt,loss})_{mass-av}$/(MFR) in Fig. 17(b) decreases significantly for Case-a and moderately for Case-b as the M increases. The ratios, $(C_{pt,loss})_{mass-av}$/(MFR) are also much smaller for Case-b than for Case-a when the blowing ratio is small, i.e. $M < 1.8$. The difference in $(C_{pt,loss})_{mass-av}$/(MFR) between the two Cases decreases when $M \geq 1.8$. The power consumed by the compressor to supply the auxiliary coolant is expected to be higher in the gas turbine cycle for the application of Case-b than for the Case-a due to the higher mass flux at a given blowing ratio. However, the lower values of $(C_{pt,loss})_{mass-av}$/(MFR) at a blowing ratio for Case-b justify the advantages of the diffused holes over the cylindrical holes in improving the aerodynamic performance of vane passage.

Figure 17(c) compares the average $C_{pt,loss}$ in percent between the present cases and Refs. [37, 38]. The denominator in Eq. (8) is replaced by $(P_{t,r} - P_{s,f})$, where $P_{s,f}$ is the local static pressure, to determine the overall $C_{pt,loss}(\%)$ in Plane-4. The data from [37, 38] are obtained for the full-coverage of film-cooling when all the endwall cooling-holes provide the film-cooling flow. The $C_{pt,loss}(\%)$ of Ref. [37] compares well with the present cases when $M < 2.2$. The values of $C_{pt,loss}(\%)$ increase with the M in Ref. [37] as the mixing losses of the coolant become significant at higher blowing ratios. The data form Ref. [38] decrease as the M increases and are smaller than the present $C_{pt,loss}(\%)$ because the three-dimensional endwall [38] reduces the passage vortex strength significantly.

E. Adiabatic film-cooling effectiveness, η

The film-cooling flow distributions along the endwall and the effective thermal protection of endwall from the mainstream gas are indicated by the local film-cooling effectiveness distributions on endwall. Equation (2) defines the local adiabatic film-cooling effectiveness, η. Figures 18 and 19 show the η distributions along the endwall for Case-a and Case-b at the blowing ratios, $M = 18$ and 2.2. The apparent locations of the cooling hole-exits, vane leading-edge, vane pressure-side (PS), and vane suction-side (SS) on the endwall are identified in Fig. 18. Also, the "Separation lines" are drawn in Fig. 18 based on the results of Mahmood et al. [36] to approximately locate the paths of suction side-leg vortex and pressure side-leg vortex along the boundary layer separations. Mahmood et al. [36] employ the vane profiles similar to the present ones. The

effectiveness, η is high when the local surface temperature, T_w on endwall is low signifying good protection and less heat transfer on endwall locally. At exit locations of the coolant holes in Figs. 18 and 19, the η values are the highest as expected. Note that the individual coolant streaks from the holes are not apparent in the η distributions downstream of holes for the neighboring coolant streaks interact with each other as they issue from the densely populated holes. For Case-a in Figs. 18, the η distributions in the region of $0.0 < X_G/C_{ax} < 0.45$ are approximately uniform between the "Separation lines", higher near the SS, and lower near the PS. The η distributions in $0.0 < X_G/C_{ax} < 0.3$ in Fig. 18 for Case-b between the "Separation lines" have higher values than for Case-a. The η values in Fig. 18 are also higher downstream of the "Separation lines" toward the SS for Case-b than for Case-a. The differences in η distributions between Case-a and Case-b concur with the results of θ previously as the more coolant mass migrates and is lost into the boundary layer for Case-a. With the increase in $M = 2.2$ in Fig. 19, the values of η increase along endwall for both the Cases. The distributions of η at $M = 2.2$ also have higher values for Case-b than for Case-a especially in the region of $0.0 < X_G/C_{ax} < 0.3$. The higher values of η distributions for Case-b in Fig. 19 also occur for the higher momentum of the coolant jet distributes the film-cooling flow better along endwall.

Figure 20 compares the pitch-averaged effectiveness, $\eta_{pitch-av}$ along endwall between Case-a and Case-b at $M = 1.8$ and $M = 2.2$. The pitchwise local values of η between SS and PS at a constant X_G/C_{ax} location are averaged arithmetically to compute a local value of $\eta_{pitch-av}$. The average effectiveness along X_G/C_{ax} decreases generally in Fig. 20 as the coolant coverage diminishes downstream along endwall. The $\eta_{pitch-av}$ values are always higher notably near the passage entrance in $0.0 < X_G/C_{ax} < 0.2$ for Case-b than for Case-a at a blowing ratio. Also, the $\eta_{pitch-av}$ values increase with the M for both Cases-(a, b) at all X_G/C_{ax} locations.

The overall-average adiabatic effectiveness, η_{av} as the M varies is compared between Case-a and Case-b in Fig. 21(a). The overall η_{av} increases with the blowing ratio, M in Fig. 21(a) for both Case-a and Case-b with the higher values of η_{av} for Case-b. Refs. [20, 39] also show higher overall cooling effectiveness for the fan-shaped holes than for the cylindrical holes with little effects of the coolant flow rate on the overall effectiveness. On the contrary, the effects of coolant flow rate on the adiabatic effectiveness for the diffused hole film-cooling (Case-b) are significant. However, the distributions of overall effectiveness as the coolant flow rate increases in Barigozzi et al. [19] for the large area fan-shaped holes and in the present Case-b are similar qualitatively. The difference in η_{av} between the diffused hole and cylindrical hole decreases slightly at the highest blowing ratio of $M = 2.2$ as the amount of coolant jet lift-up from the endwall region into the mixing layer is higher for the diffused holes than for the cylindrical holes. The jet-momentum is always higher for the diffused holes (Case-a) as evidenced in Table 3 that shows the jet-momentum flux ratio, $(m_c u_c)_{diffused}/(m_c u_c)_{cylindrical}$ is always greater than 1.0. The high jet-momentum causes some coolant to lift-up from the endwall.

The ratios of overall $\eta_{av}/(MFR)$ are presented in Fig. 21(b) with the M variation. The ratio $\eta_{av}/(MFR)$ estimates the overall cooling effectiveness achieved per unit of coolant mass-fraction (MFR) spent. The values of MFR in Table 3 are used to compute $\eta_{av}/(MFR)$. The data for Case-a and Case-b are compared in Fig. 21(b). The requirement of high coolant mass-flux at high MFR increases the power load on gas-turbine compressor that supplies the coolant. The high overall η_{av} at the low coolant flow rate or M providing the high value $\eta_{av}/(MFR)$ is thus desirable for the film-cooling design. As shown in Fig. 21(b), the $\eta_{av}/(MFR)$ values for both Case-a and Case-b are very high at the low blowing ratio of $M = 1.0$ and then decrease sharply as the M increases. The values of $\eta_{av}/(MFR)$ are higher for Case-a than for Case-b at $M \leq 1.4$ and about the same for the two Cases at $M > 1.4$. The higher values of MFR at low M for Case-b are responsible for the smaller $\eta_{av}/(MFR)$ than for Case-a. The diffused hole film-cooling is superior to the cylindrical hole film-cooling for cooling the endwall only when the amount of coolant spent is not considered. However, the requirement of higher coolant flow rate may outweigh the benefits of higher film-cooling effectiveness of the diffused holes. The average jet-momentum flux ratio of diffused hole mass flow rate to cylindrical hole mass flow rate is also included in Table 3. The average jet-momentum flux ($m_c u_c$) of each coolant hole is obtained based on the total coolant flow rate, M_c and number of cooling holes. The average momentum flux ratio in Table 3 is always higher than 1.0 signifying the jet-momentum for the diffused hole is higher than for the cylindrical hole.

Figure 22 provides comparisons between the present overall effectiveness, η_{av} values and area-averaged η_{av} in Refs. [4, 40] as the MFR(%) varies. The data of [4, 40] are obtained for the cases with film-cooling flow from the upstream slots and holes. The effects of the density ratio on the data of [4, 40] are insignificant. For all the cases in Fig. 22, the η_{av} value increases with the MFR(%). The present η_{av} values are slightly higher than the area-averaged data in [4, 40] because of the arithmetic averaging of the local values for the present data.

IV.   Conclusion

Film-cooling performances of the cylindrical holes and diffused cylindrical holes are experimentally measured and compared in an atmospheric linear vane cascade. The film-cooling holes are employed in the pitchwise rows in the endwall slightly upstream of the cascade inlet. The diffused cylindrical holes are designed by diffusing the cylindrical holes in the forward direction smoothly. The inlet Reynolds number to the cascade is 2.0E+05. The coolant-to-mainstream density ratio for all the tests is about 1.0 when the temperature ratio is varied between 0.94 and 1.0. The tests are conducted for four inlet blowing ratios of the film-cooling flow. The results are compared in four pitchwise planes between the cylindrical holes and diffused cylindrical holes.

The distributions of the non-dimensional temperature in the test planes reveal that the coolant streams migrate more into the boundary layer, concentrate more toward the passage suction-side, and are lifted-up higher above endwall by the suction

side-leg vortex for the cylindrical hole than for the diffused hole. The higher momentum of coolant of the diffused hole film-cooling adjacent to endwall is responsible for better coolant distributions along endwall. The values of non-dimensional flow temperature adjacent to endwall are thus lower for the diffused holes compared to those for the cylindrical holes. The streamline velocity distributions in the pitchwise plane located half-way inside the passage show more coolant penetrates and it is lost into the boundary layer for the cylindrical holes than for the diffused holes. The yaw-angle distributions in the mid-passage plane show less turning of the coolant streams for the cylindrical holes than for the diffused holes.

The distributions of the total-pressure loss coefficients in the cascade exit plane indicate that the total-pressure losses are lower for the diffused holes than for the cylindrical holes. The weaker passage vortex and less mixing of coolant with the boundary layer fluid reduce the total-pressure losses across the cascade for the diffused hole film-cooling. The aerodynamic losses across the gas-turbine passages are then expected to be low when the diffused hole film-cooling is employed.

The distributions of adiabatic film-cooling effectiveness on the endwall show the coolant coverage of endwall is better for the diffused holes than for the cylindrical holes. The overall cooling effectiveness increases with the blowing ratio for both types of holes, but it is always higher for the diffused holes. However, the mass-flux of coolant also increases with the blowing ratio. The high overall film-cooling effectiveness for the diffused holes is caused at the expense of high film-cooling flow rate. Compared to the cylindrical hole film-cooling, the present arrangement of diffused cylindrical hole film-cooling thus has the potential to provide better aerodynamic performance and higher film-cooling effectiveness, but at the higher loads on the compressor when employed in the actual gas-turbine. The results of the investigation can be the basis of any future investigations of the flow-field in the film-cooled cascade and will benefit the film-cooling design of the gas-turbine passages.

Acknowledgments

References

[1] Werschnik, H., Ostrowski, T., Hilgert, J., Schneider, M., and Schiffer, H.-P., "Infrared thermography to study endwall cooling and heat transfer in turbine stator vane passages using the auxiliary wall method and comparison to numerical simulations," *Quantitative InfraRed Thermography Journal,* Vol. 12, No. 2, 2015, pp. 219-236.

URL: https://doi.org/10.1080/17686733.2015.1066135.

[2] Thomas, M., and Povey, T., "Improving turbine endwall cooling uniformity by controlling near-wall secondary flows," *Proceedings of the Institution of Mechanical Engineers, Part G: J. Aerospace Engineering*, Vol. 231, No.14 , 2016, pp. 2689-2705.

DOI: 10.1177/0954410016673092.

[3] Ornano, F., and Povey, T., "Experimental and computational study of the effect of momentum-flux ratio on high-pressure nozzle guide vane endwall cooling systems," *Journal of Turbomachinery*, Vol. 139, No.12, 2017, pp. 1210021-12100214.

DOI: 10.1115/1.4037756.

[4] Wang, N., Shiau, C. -C., Han, J. -C., Xu, H., and Fox, M., "Turbine vane endwall film cooling from mid-chord or downstream rows and upstream coolant injection," *International Journal of Heat and Mass Transfer,* Vol. 133, 2019, pp. 247-255.

URL: https://doi.org/10.1016/j.ijheatmasstransfer.2018.12.079.

[5] Li, X., Ren, J., and Jiang, H., "Film cooling effectiveness distribution of cylindrical hole injections at different locations on a vane endwall," *International Journal of Heat and Mass Transfer*, Vol. 90, 2015, pp. 1-14.

URL: http://dx.doi.org/10.1016/j.ijheatmasstransfer.2015.06.026.

[6] Li, X., Ren, J., and Jiang, H., "Multi-row film cooling characteristics on a vane endwall," *International Journal of Heat and Mass Transfer*, Vol. 92, 2016, pp. 23-33.

URL: http://dx.doi.org/10.1016/j.ijheatmasstransfer.2015.08.049.

[7] Du, K., Song, L., Li, J., and Sunden, B., "Effects of the layout of film holes near the vane leading edge on the endwall cooling and phantom cooling of the vane suction side surface," *Numerical Heat Transfer, Part A: Applications*, Vol. 71, No. 9, 2017, pp. 910-927.

URL: http://doi.org/10.1080/10407782.2017.1326788.

[8] Thole, K. A., and Knost, D. G., "Heat transfer and film-cooling for the endwall of a first stage turbine vane," *International Journal of Heat and Mass Transfer, Vol.* 48, No. 25-26, 2005, pp. 5255-5269.

URL: http://doi.org/10.1016/j.ijheatmasstransfer.2005.07.036.

[9] Zhang, L. J., and Jaiswal, R. S., "Turbine nozzle endwall film cooling study using pressure-sensitive pain," *Journal of Turbomachinery*, Vol. 123, 2001, pp. 730-738.

URL: http:// DOI: 10.1115/1.1400113.

[10] Kost, F., and Nicklas, M., "Film-cooled turbine endwall in a transonic flow field: Part I- aerodynamic measurement," *Journal of Turbomachinery*, Vol. 123, 2001, pp. 709-719.

DOI: 10.1115/1.1400112.

[11] Nicklas, M., "Film-cooled turbine endwall in a transonic flow field: Part II- heat transfer and film-cooling effectiveness," *Journal of Turbomachinery*, Vol. 123, 2001, pp. 720-729.

DOI: 10.1115/1.1397308.

[12] Du, K., Li, Z., and Li, J., "Effects of the leading edge injection slot on the film cooling and heat transfer performance," *International Journal of Heat and Mass Transfer*, Vol.102, 2016, pp.1308-1320.

URL: http://dx.doi.org/10.1016/j.ijheatmasstransfer.2016.07.033.

[13] Du, K., and Li, J., "Numerical study on the effects of slot injection configuration and endwall alignment mode on the film cooling performance of vane endwall," *International Journal of Heat and Mass Transfer,* Vol. 98, 2016, pp.768-777.

URL: http://dx.doi.org/10.1016/j.ijheatmasstransfer.2016.02.014.

[14] Sundaram, N., and Thole, K. A. "Film-cooling flowfields with trenched holes on an endwall," *Journal of Turbomachinery*, Vol. 131, No.4, 2009, pp.0410071-04100710.

URL: https://doi.org/10.1115/1.3068316.

[15] Barigozzi, G., Abdeh, H., Perdichizzi, A., Henze, M., and Krueckels, J., "Aerothermal performance of a nozzle vane cascade with a generic nonuniform inlet flow condition- Part II: Influence of purge and film cooling injection," *Journal of Turbomachinery*, Vol. 139, 2017, pp.1010041-1010049.

DOI: 10.1115/1.4036437.

[16] Yang, X., Liu, Z., Liu, Zh, Simon, T., and Feng, Z, "Endwall film cooling performance for a first-stage guide vane with upstream combustor walls and inlet injection," *Journal of Thermal Science and Engineering Applications,* Vol. 11, 2019, pp.0110081-01100811.

DOI: 10.1115/1.4041342.

[17] Kunze, M., Vogeler, K., Brown, G., Prakash, C., and Landis, K., "Aerodynamic and endwall film-cooling investigations of a gas turbine nozzle guide vane applying temperature-sensitive paint," *Journal of Turbomachinery*, Vol. 133, No. 3, 2011, pp. 0310271-0310279.

DOI: 10.1115/1.4003426.

[18] Zhang, Y., Yuan, X., and Ligrani, P., "Film cooling effectiveness distribution on first-stage vane endwall with and without leading-edge fillets," *International Jornal of Heat and Mass Transfer*, Vol. 66, 2013, pp. 642-654.

URL: http://dx.doi.org/10.1016/j.ijheatmasstransfer.2013.06.065.

[19] Barigozzi, G., Franchini, G., and Perdichizzi, A., "End-wall film cooling through fan-shaped holes with different area ratios," *Journal of Turbomachinery*, Vol. 129, No. 2, 2007, pp. 212-220.

DOI: 10.1115/1.2464140.

[20] Colban, W., Thole, K. A., and Haendler, M., "A comparison of cylindrical and fan-shaped film-cooling holes on a vane endwall at low and high freestream turbulence levels," *Journal of Turbomachinery*, Vol. 130, No. 3, 2008, pp. 0310071-0310079.

DOI: 10.1115/1.2720493.

[21] Yang, X., Zhao, Q., and Feng, Z., "Experimental evaluation of cooling effectiveness from novel film holes over turbine endwalls with inlet swirl," *International Journal of Thermal Sciences,* Vol. 174, 2022, pp. 107434 (1-17).
URL: https://doi.org/10.1016/j.ijthermalsci.2021.107434.

[22] Seo, H.J., Park, S.H., Kwak, and Kang, Y.S., "Experimental and numerical study on the effect of fan-shaped hole configuration on film cooling effectiveness", *ASME Turbo Expo Proceeding, ASME paper GT2019-90817,* V05BT19A013.
URL: https://doi.org/10.1115/GT2019-90817.

[23]. Timko, L.P, "Energy Efficient Engine High Pressure Turbine Component Test Performance," NASA CR-168289, 1984.

[24] Arnachellan, K., "Aerodynamic Loss Reduction in a Vane Cascade With Leading-Edge Fillet and Upstream Endwall Film-Cooling," MEng. Thesis, Mechanical and Aeronautical engineering, University of Pretoria, Pretoria, South Africa, 2017.

[25] Mahmood, G. I., and Arnachellan, K., "Effects of upstream endwall film-cooling on a vane cascade flow-field," *Journal of Propulsion and Power*, Vol. 34, No 2, 2018, pp. 460-468.
DOI: 10.2514/1.B36640.

[26] Li, W., Li, X, Ren, J., and Jiang, H., "A novel method for designing fan-shaped holes with short length-to-diameter ratio in producing high film cooling performance for thin-wall turbine airfoil," *Journal of Turbomachinery*, Vo. 140, No. 9, 2018, pp. 0910041-09100415.
URL: https://doi.org/10.1115/1.4041035.

[27] Li, Y., Zhang, Y., Su, X., and Yuan, X., "Experimental and numerical investigations of shaped hole film cooling with the influence of endwall cross flow," *International Journal of Heat and mass Transfer,* Vol. 120, 2018, pp. 42-55.
URL: https://doi.org/10.1016/j.ijheatmasstransfer.2017.11.150.

[28]. Gritsch, M, Colban, W., Schär, H., and Döbbeling, K., "Effect of hole geometry on the thermal performance of fan-shaped film cooling holes," *Journal of Turbomachinery*, Vol. 127, No. 4, 2005, pp. 718-725.
URL: https://doi.org/10.1115/1.2019315.

[29] Schroeder, R. P., and Thole, K. A, "Adiabatic effectiveness measurements for a baseline shaped film cooling hole," *ASME Turbo Expo Proceeding*, ASME paper GT2014-25992, 2014.
URL: https://doi.org/10.1115/GT2014-25992.

[30] Aghasi, P., Gutmark, E., and Munday, D., "Dependence of film cooling effectiveness on three-dimensional printed cooling holes," *Journal of Heat Transfer*, Vol. 139, 2017, pp. 1020031-10200315.
DOI: 10.1115/1.4036509.

[31] Bell, C. M., Hamakawa, H., and Ligrani, P. M., "Film cooling from shaped holes," *Journal of Heat Transfer*, Vol. 122, No 2, 2000, pp. 224-232.
URL: https://doi.org/10.1115/1.521484.

[32] Shote, A. S., Mahmood, G. I., and Meyer, J. P., "Influences of large fillets on endwall flows in a vane cascade with upstream slot film-cooling," *Exerimental Thermal and Fluid Science*, Vol. 112, 2020, pp. 109951.
URL: http://dx.doi.org/10.1016/j.expthermflusci.2019.109951.

[33] Sargent, S. R., Hedlund, C. R., and Ligrani, P. M., "An infrared thermography imaging system for convective heat transfer measurements in complex flows," *Measurement Science and Technology*, Vol. 9, No. 12 ,1998, pp. 1974-1981.

URL: https://doi.org/10.1088/0957-0233/9/12/008.

[34] Moffat, R. J., "Describing the uncertainties in experimental results," *Experimental and Thermal and Fluid Science*, Vol. 1, No. 1, 1988, pp. 3-17.

URL: https://doi.org/10.1016/0894-1777(88)90043-X.

[35] Beckwith, T. G, Marangoni, R. D., and Lienhard, J. H, *Mechanical Measurements*, *6th* ed., Pearson Prentice Hall, New Jersey, 2007, pp. 42-45, 54-59.

[36] Mahmood, G. I., Saha, A. K., and Acharya, S., "Secondary flows and upstream film cooling in a linear NGV cascade in compressible flows: computations and experiments," *6th International Conference on Heat Transfer, Fluid Mechanics and Thermodynamic*s, HEFAT 2008, Paper no. MG1.

[37] Friedrichs, S., Hodson, H. P., and Dawes, W. N., "Aerodynamics aspects of endwall film cooling", *Journal of Turbomachinery,* Vol. 119, No. 4, 1997, pp. 786-793.

URL: https://doi.org/10.1115/1.2841189.

[38] Gustafson, R., Mahmood, G. I., and Acharya, S, "Flowfield in a film-cooled three-dimensional contoured endwall passage: aerodynamic measurements"*, ASME Turbo Expo: Power for Land, Sea, and Air*, 2007.

DOI: 10.1115/GT2007-28154.

[39] Wang, J., Tian, K., Luo, J., and Sundén, B., "Effect of hole configurations on film cooling performance", *Numerical Heat Transfer,* Part A: Applications, Vol. 75, No. 11, 2019, pp. 725-738.
URL: https:// DOI: 10.1080/10407782.2019.1608762.

[40] Yang, X., Zhao, Q., Liu, Z., Zhao, L., and Feng, Z., "Film cooling patterns over an aircraft engine turbine endwall with slot leakage and discrete hole injection", *International Journal of Heat and mass Transfer,* Vol. 165, PartA, 2021, pp. 120565 (1-17).

URL: https://doi.org/10.1016/j.ijheatmasstransfer.2020.120565.

Table 1 Geometric parameters of vane cascade

Incidence	Exit angle	C_{ax} (m)	C (m)	C/S	C/P
$0°$	74°	0.203	0.355	1.479	1.328

Table 2 Reference flow-parameters (2.5C_{ax} upstream of cascade)

Freestream velocity, U	10.0 m/s
Static pressure, $P_{s,r}$ ("-ve" gage)	60 Pa
Velocity boundary layer thickness, δ/S	10%
Streamwise (freestream) turbulence intensity	3%
Temperature (T_r), density (ρ_r)	298 K, 1.02 kg/m^3
Coolant to reference density ratio ($\rho_{c,b}/\rho_r$):	1.0
Coolant to reference temperature ratio ($T_{c,b}/T_r$):	1.0 - 0.94
Reynolds number, Re	2.0E+05

Table 3 MFR (M_c/M_a) of coolant to passage flow and jet-momentum flux ratio of coolant flows

M	2.4	2.2	1.8	1.0
MFR, Case-a (Cylindrical)	0.048425	0.041188	0.009999	0.001530
MFR, Case-b (Diffused)	0.058698	0.043775	0.018970	0.002139
$(m_c u_c)_{diffused}/(m_c u_c)_{cylindrical}$	2.21	1.70	5.42	2.94
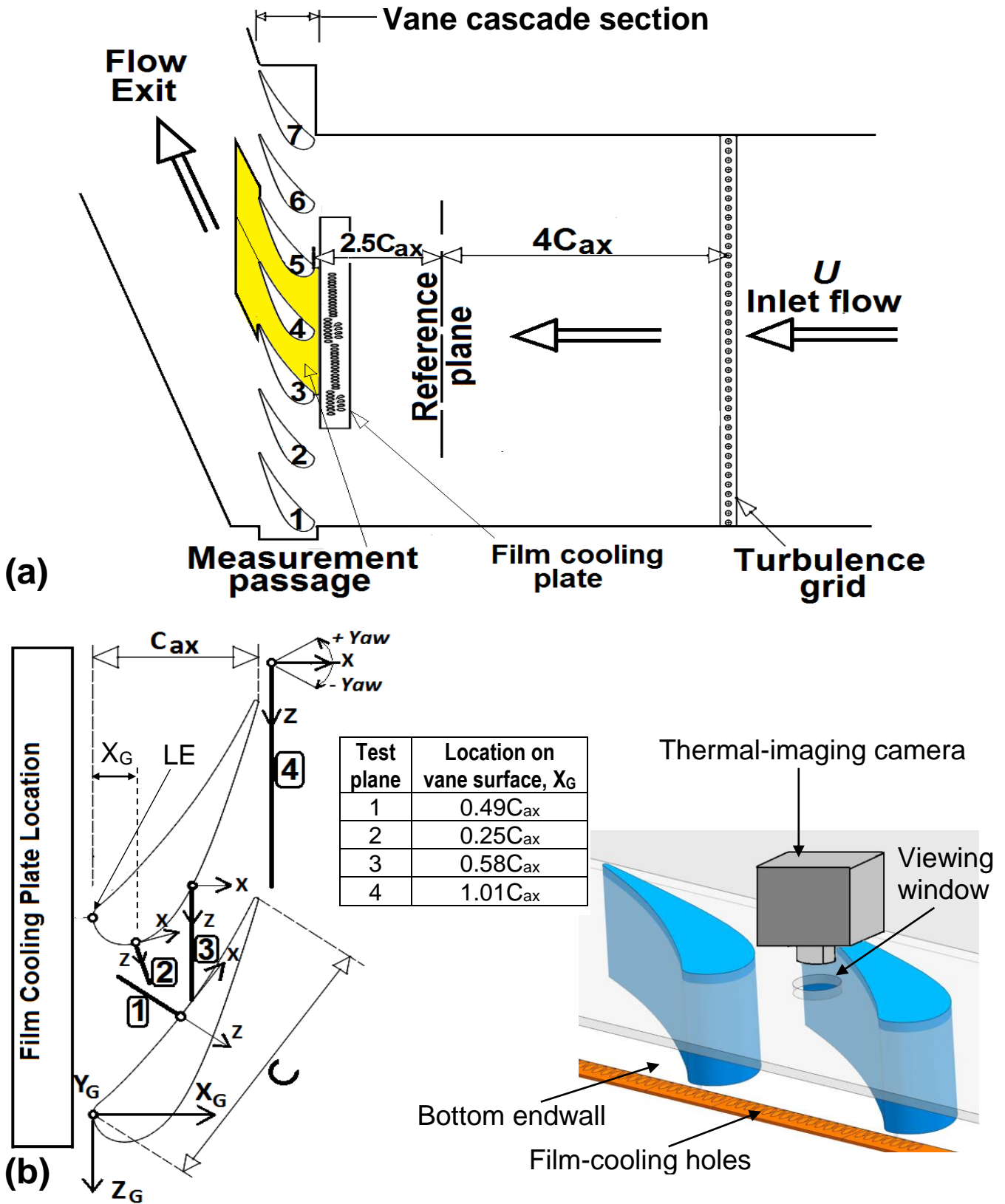
Fig. 1 (a) Plan view of the cascade test facility in wind tunnel, and (b) Vane profile with measurement locations and coordinates in the passage between vane-3 and vane-4.
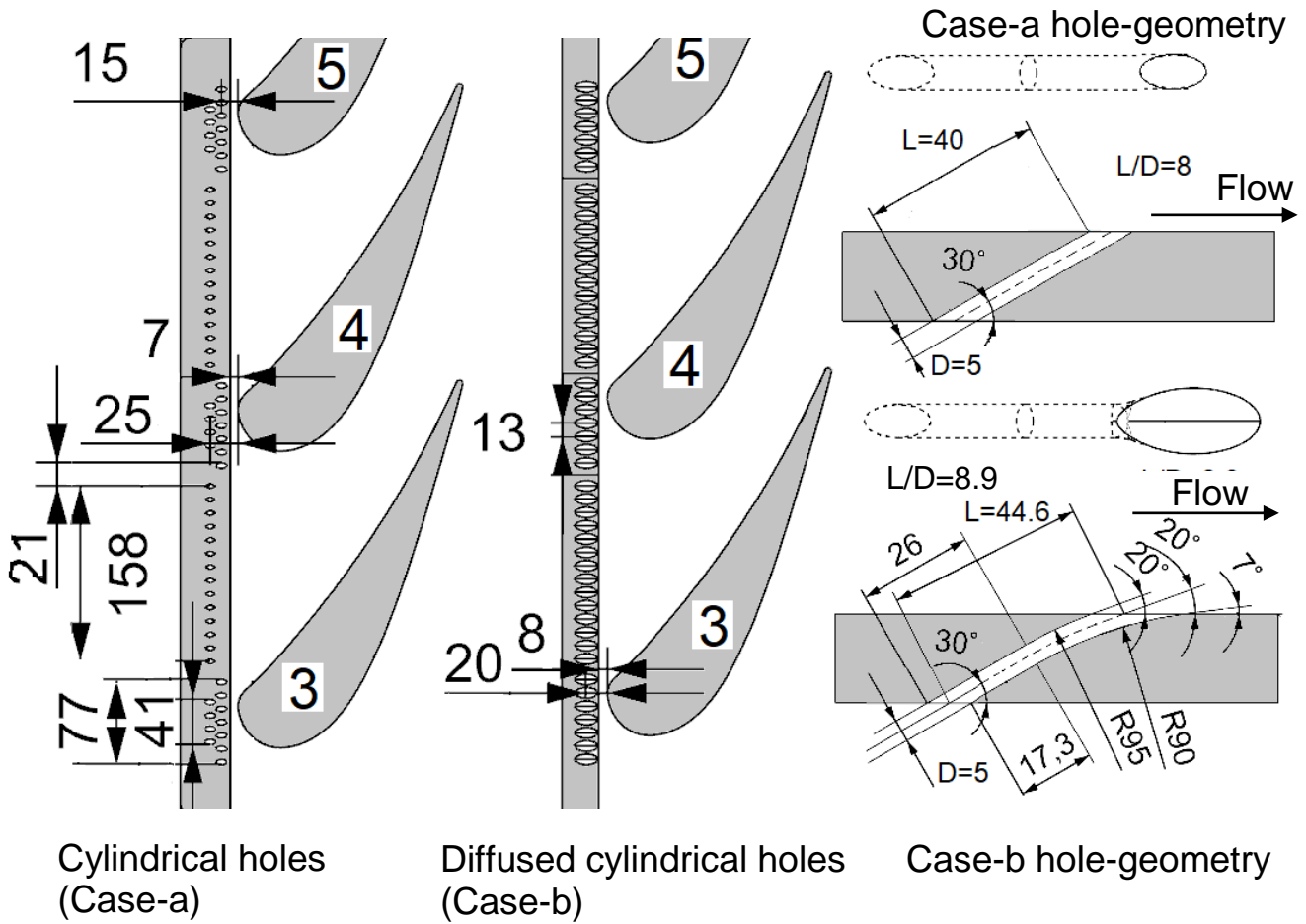
Fig. 2 Two film-cooling hole geometries and arrangements in the film cooling plate: Case-a (Cylindrical holes) and Case-b (Diffused cylindrical holes). All dimensions shown are in mm.
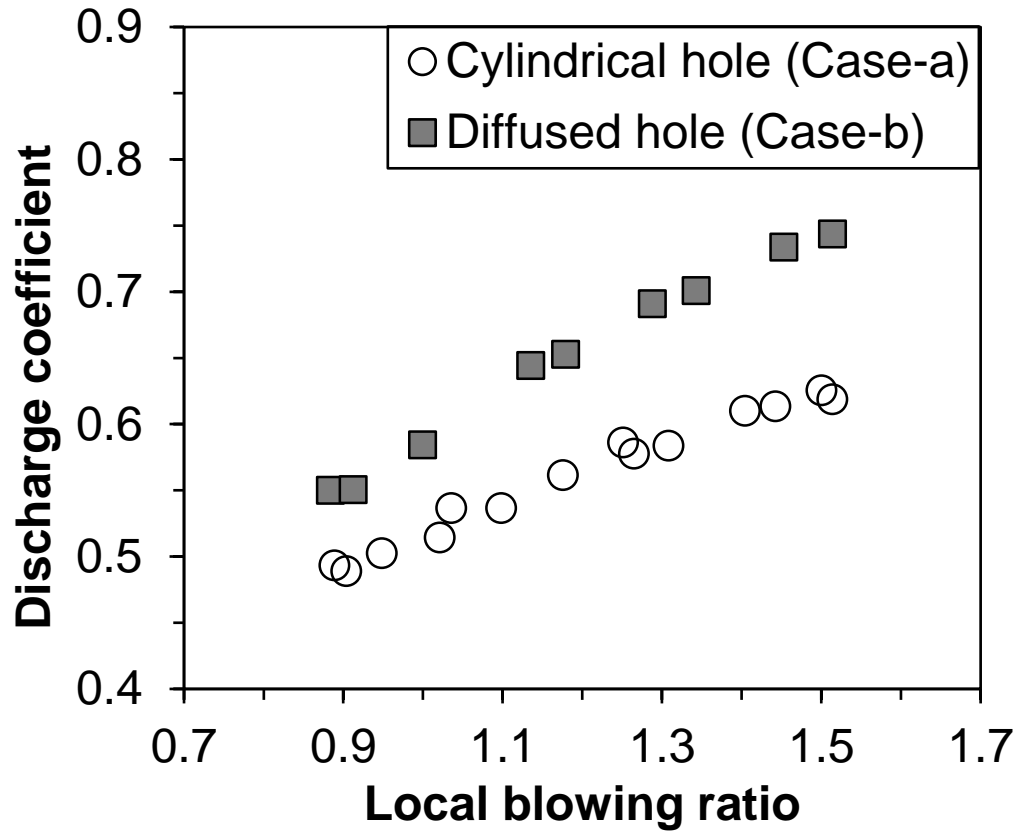
Fig. 3 Discharge coefficients at different local blowing ratios for cylindrical hole and diffused cylindrical hole at 0° compound angle in a smooth wind tunnel,
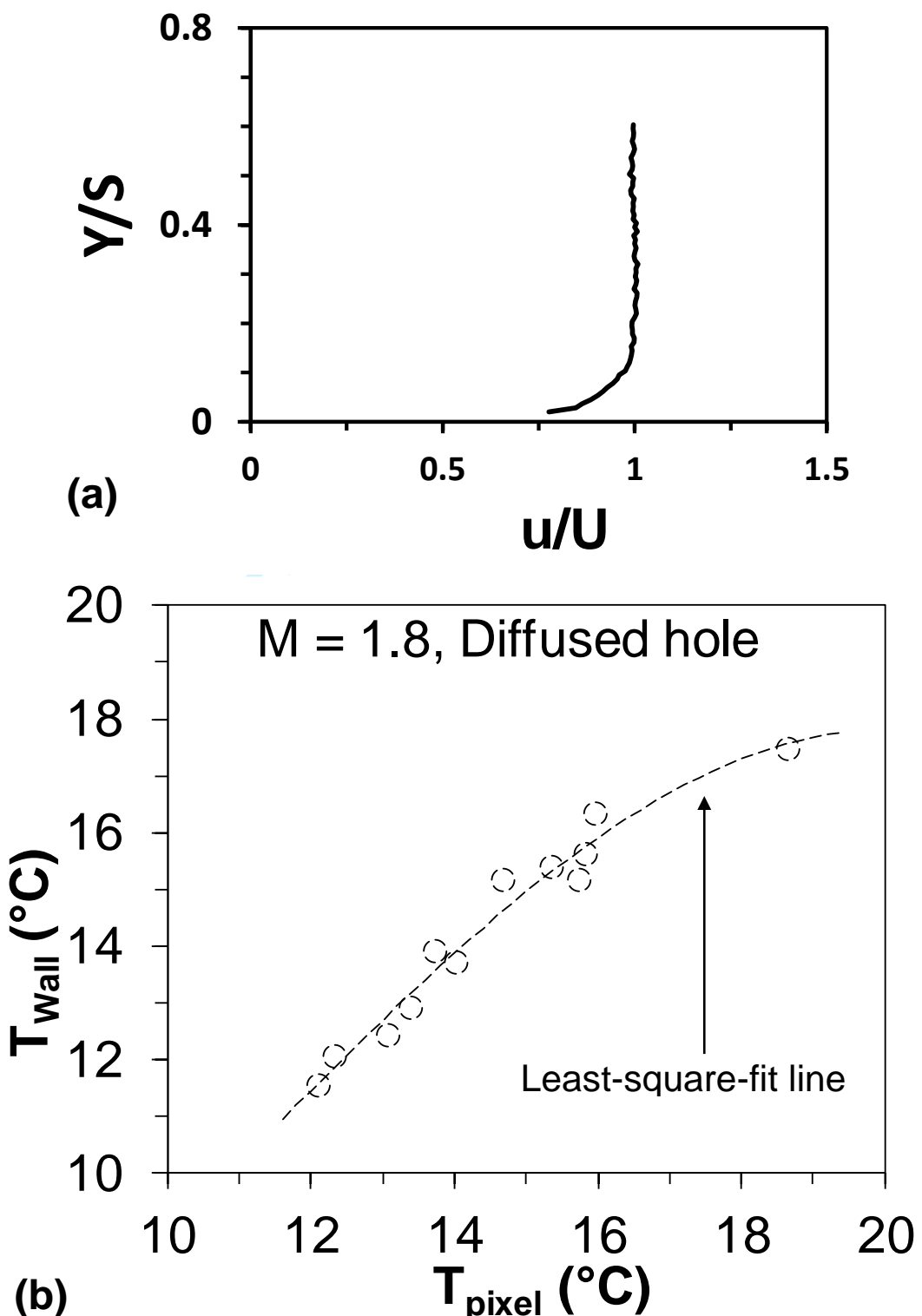
Fig. 4: (a) Streamwise velocity profile at reference plane, and (b) In-situ calibration plot of thermal-image pixel temperatures, T_{pixel} (°C) with thermocouple temperatures, T_{wall} (°C) on test endwall at M = 1.8 for Case-b (diffused holes).
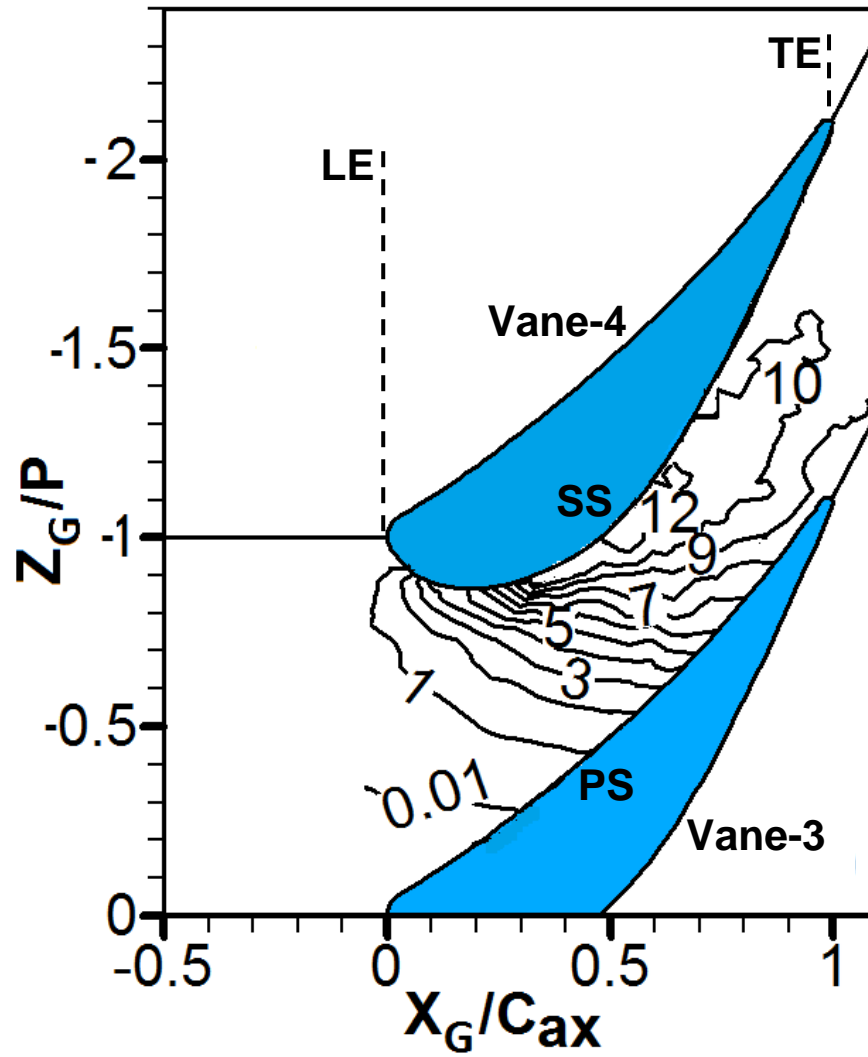
Fig. 5 Wall-pressure coefficient, $C_{p,w}$ distribution along endwall of vane passage without any film-cooling flow (baseline case).
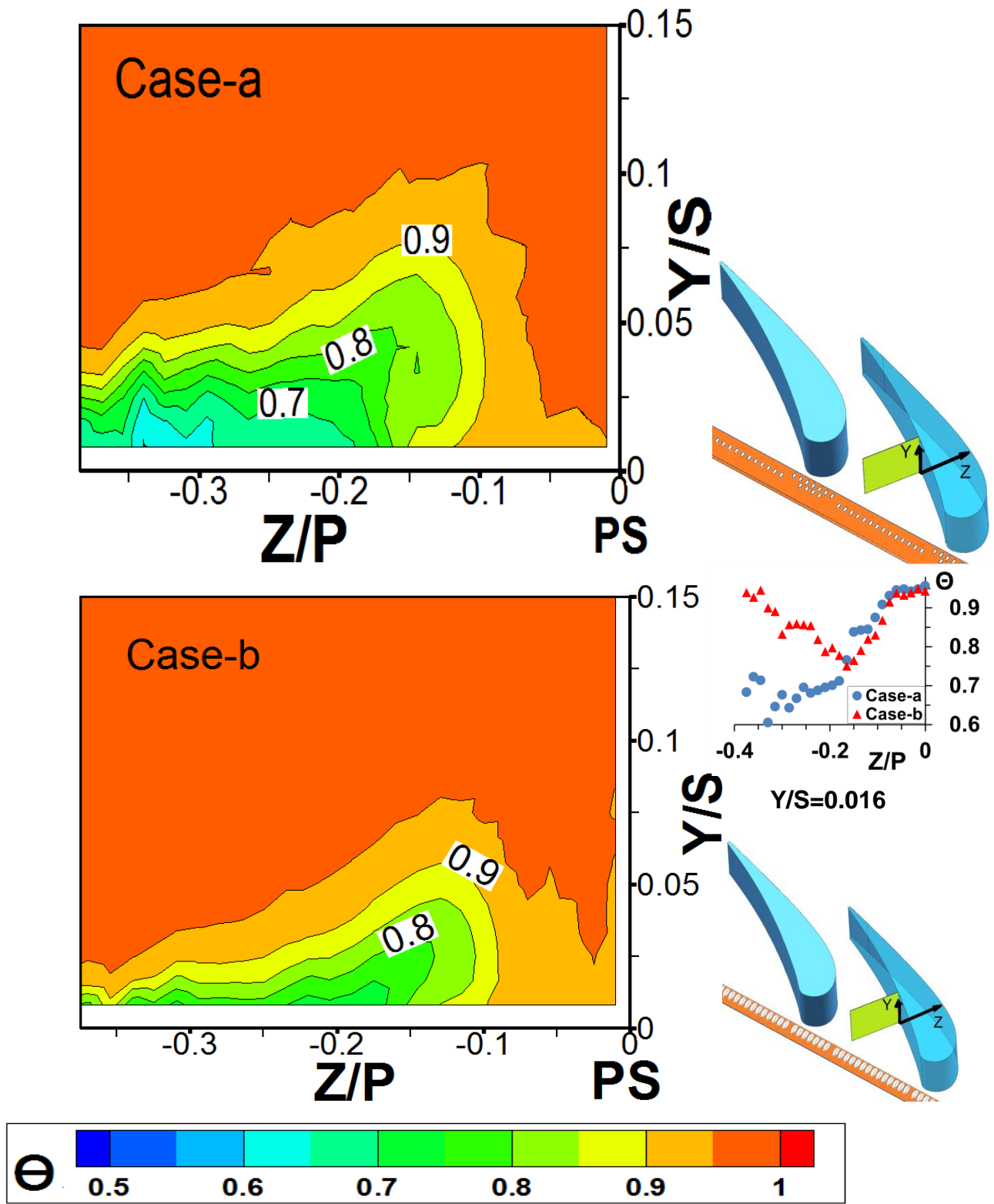
Fig. 6 Distributions of non-dimensional temperature, θ in Plane-1 for Cases-(a, b) at M=1.8.
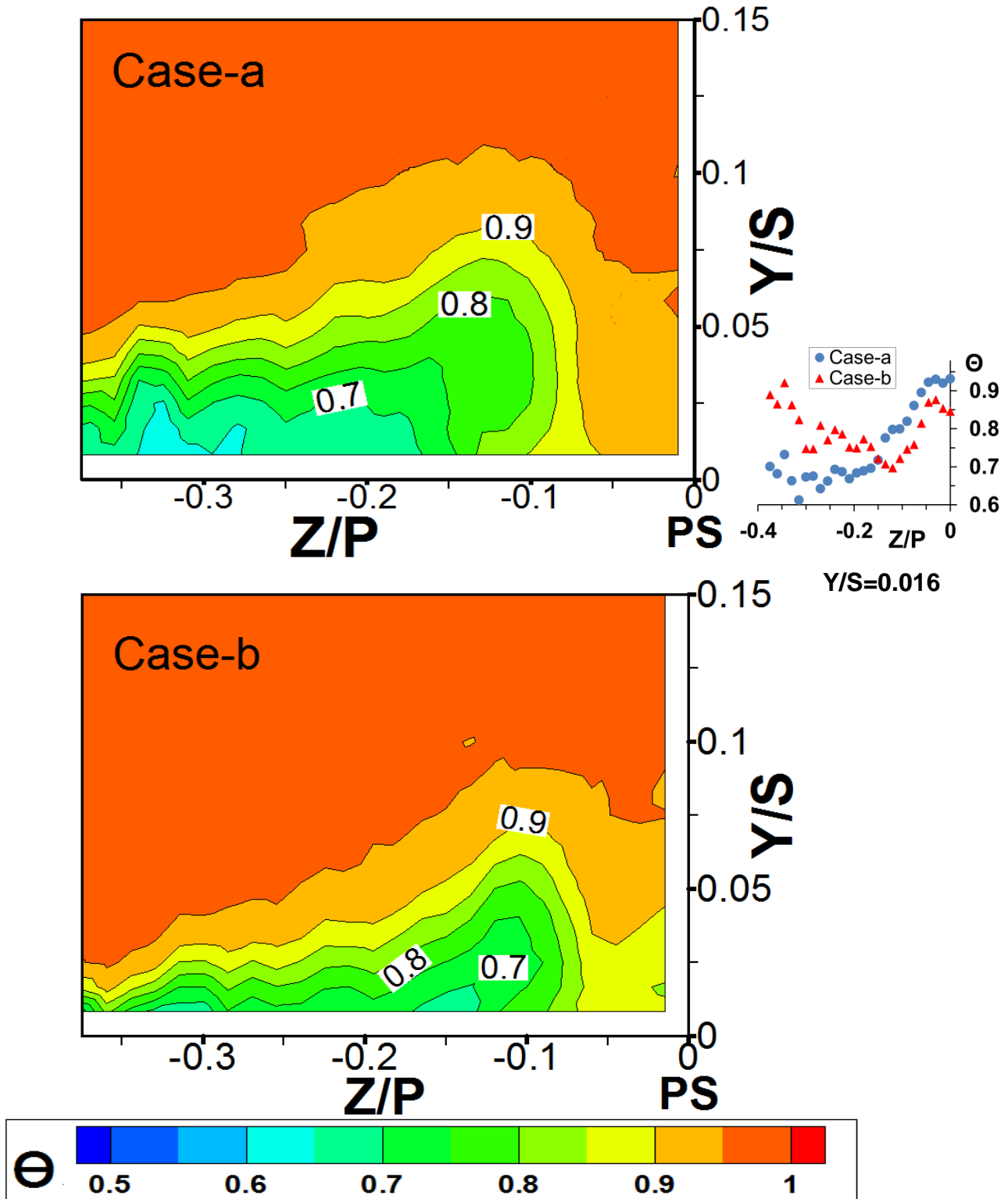
Fig. 7 Distributions of non-dimensional temperature, θ in Plane-1 for Cases-(a, b) at M=2.2.
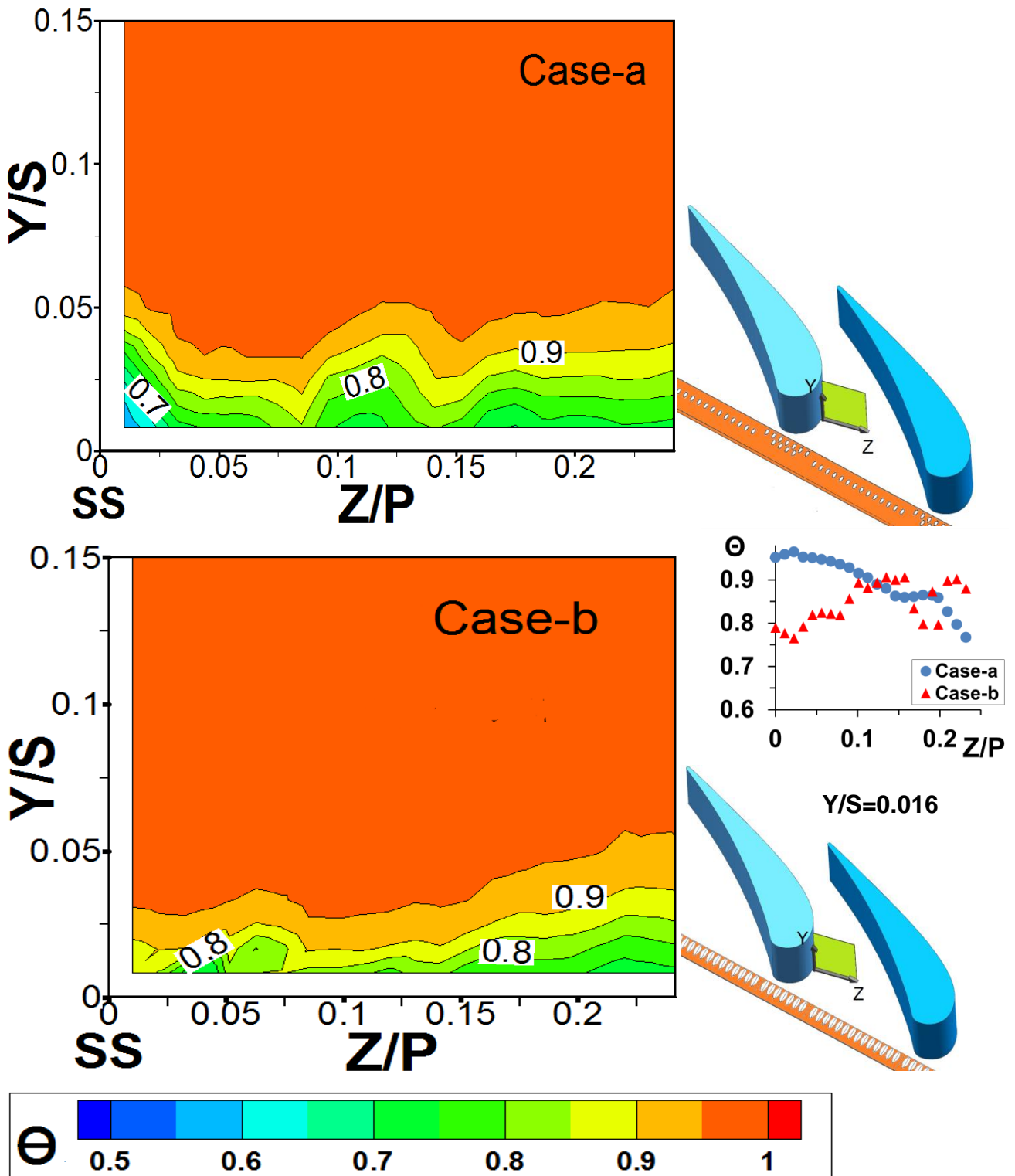
Fig. 8 Distributions of non-dimensional temperature, θ in Plane-2 for Cases-(a, b) at M=1.8.
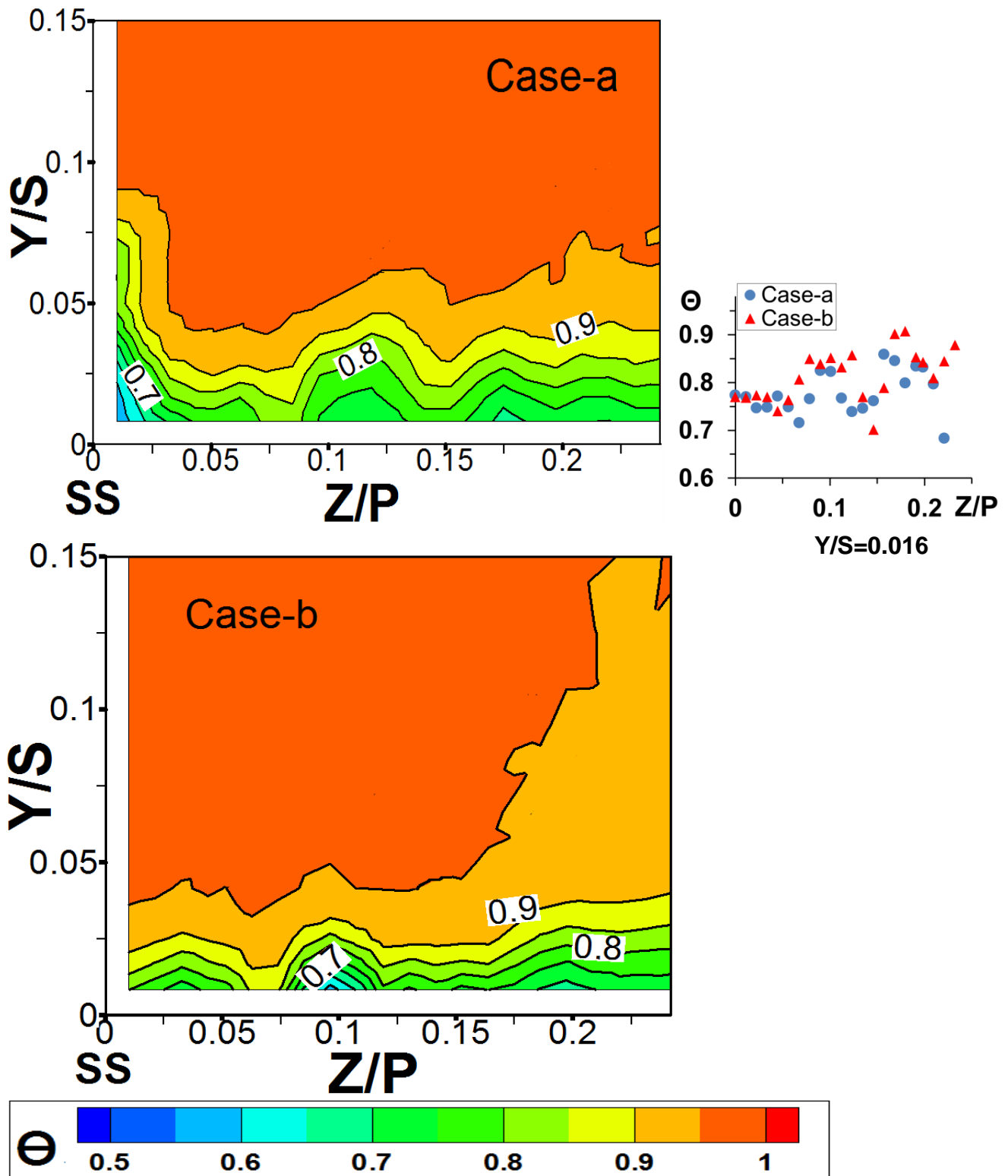
Fig. 9 Distributions of non-dimensional temperature, θ in Plane-2 for Cases-(a, b) at M=2.2.
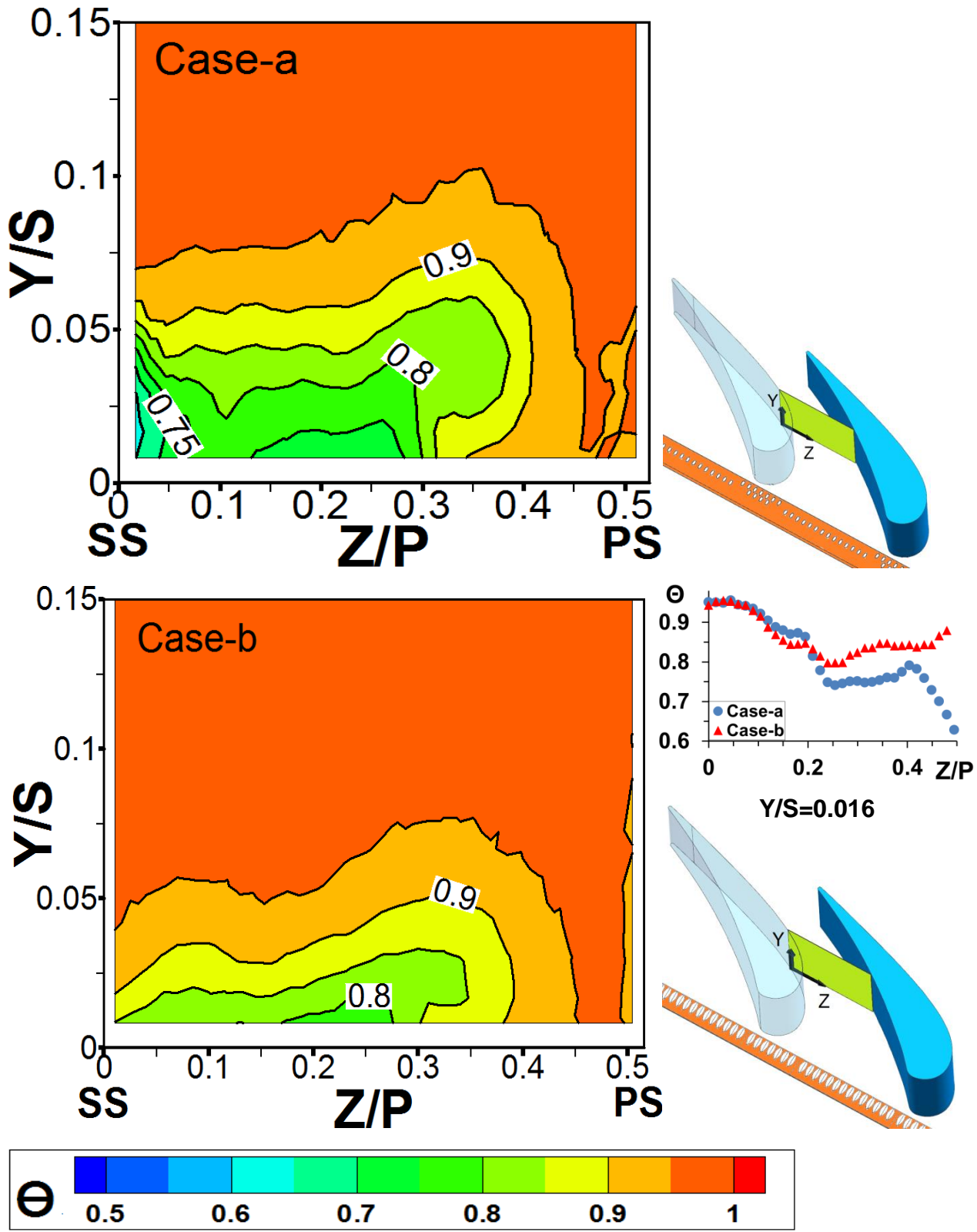
Fig. 10 Distributions of non-dimensional temperature, θ in Plane-3 for Cases-(a, b) at M=1.8.
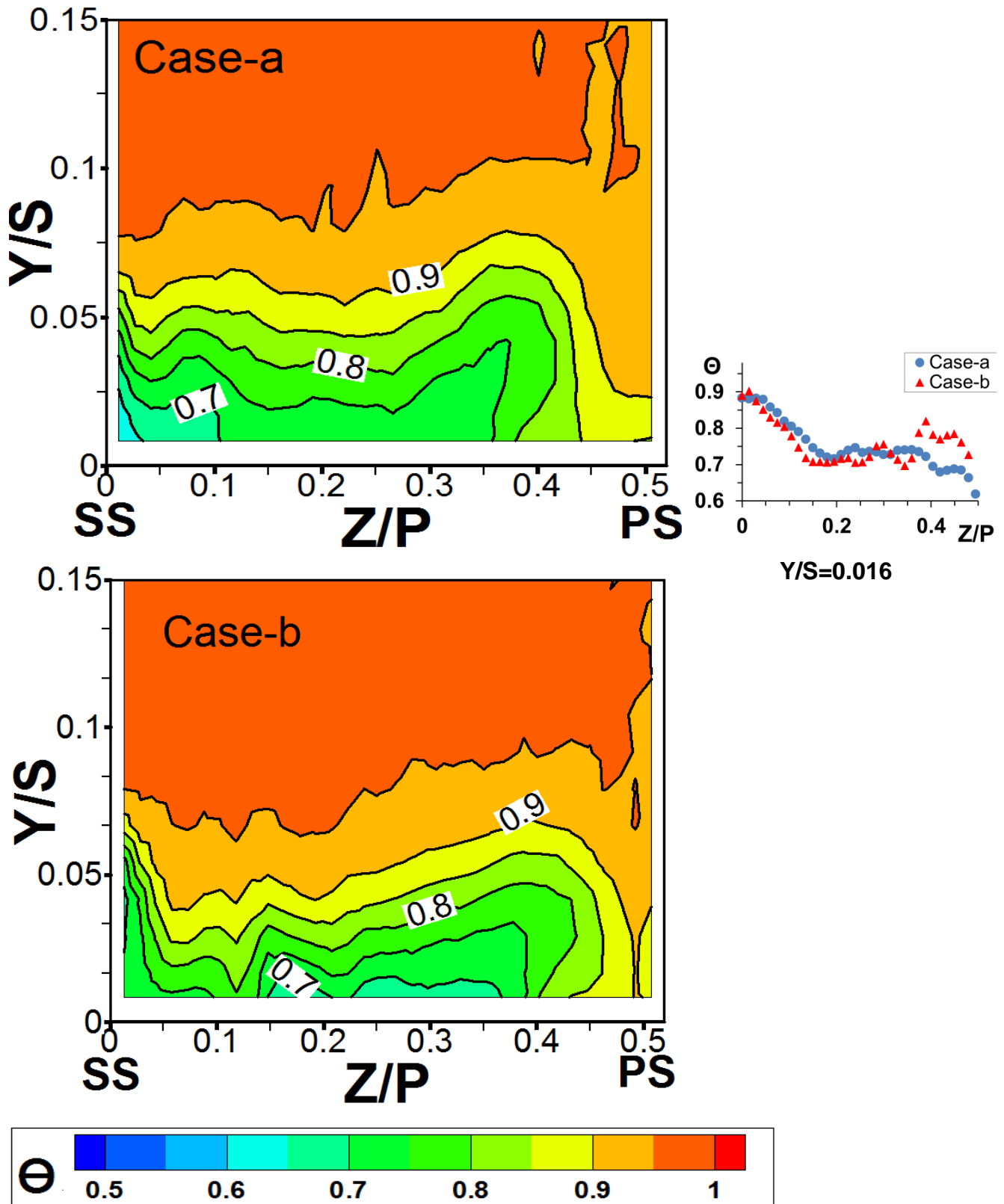
Fig. 11 Distributions of non-dimensional temperature, θ in Plane-3 for Cases-(a, b) at M=2.2.
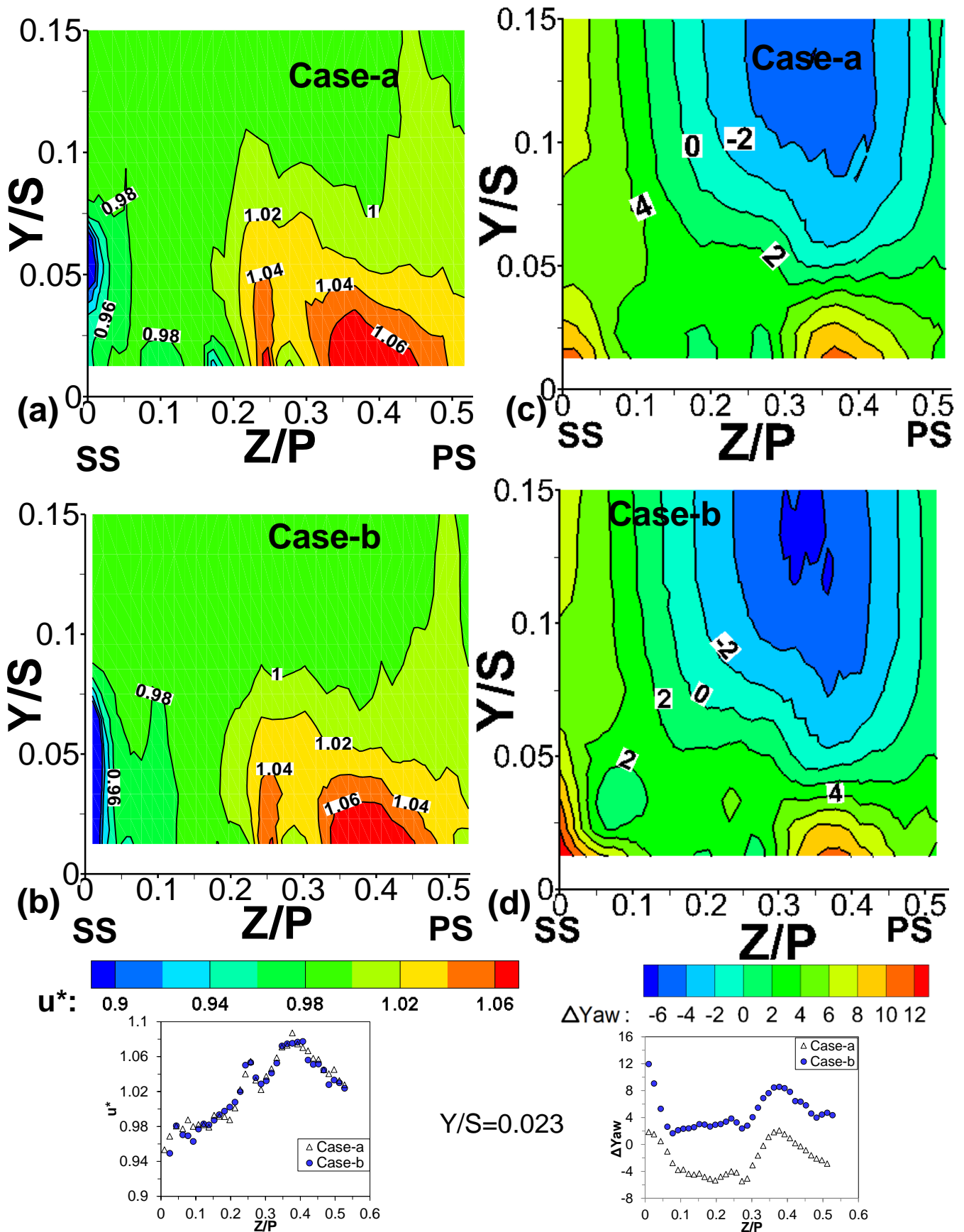
Fig. 12 Distributions of streamline velocity ratio, u* (a, b) and flow yaw-angle deviation (deg), ΔYaw (c, d) near endwall in Plane-3 for Cases-(a, b) at M=1.8. Data in line plots at the bottom are shown at location Y/S=0.023.
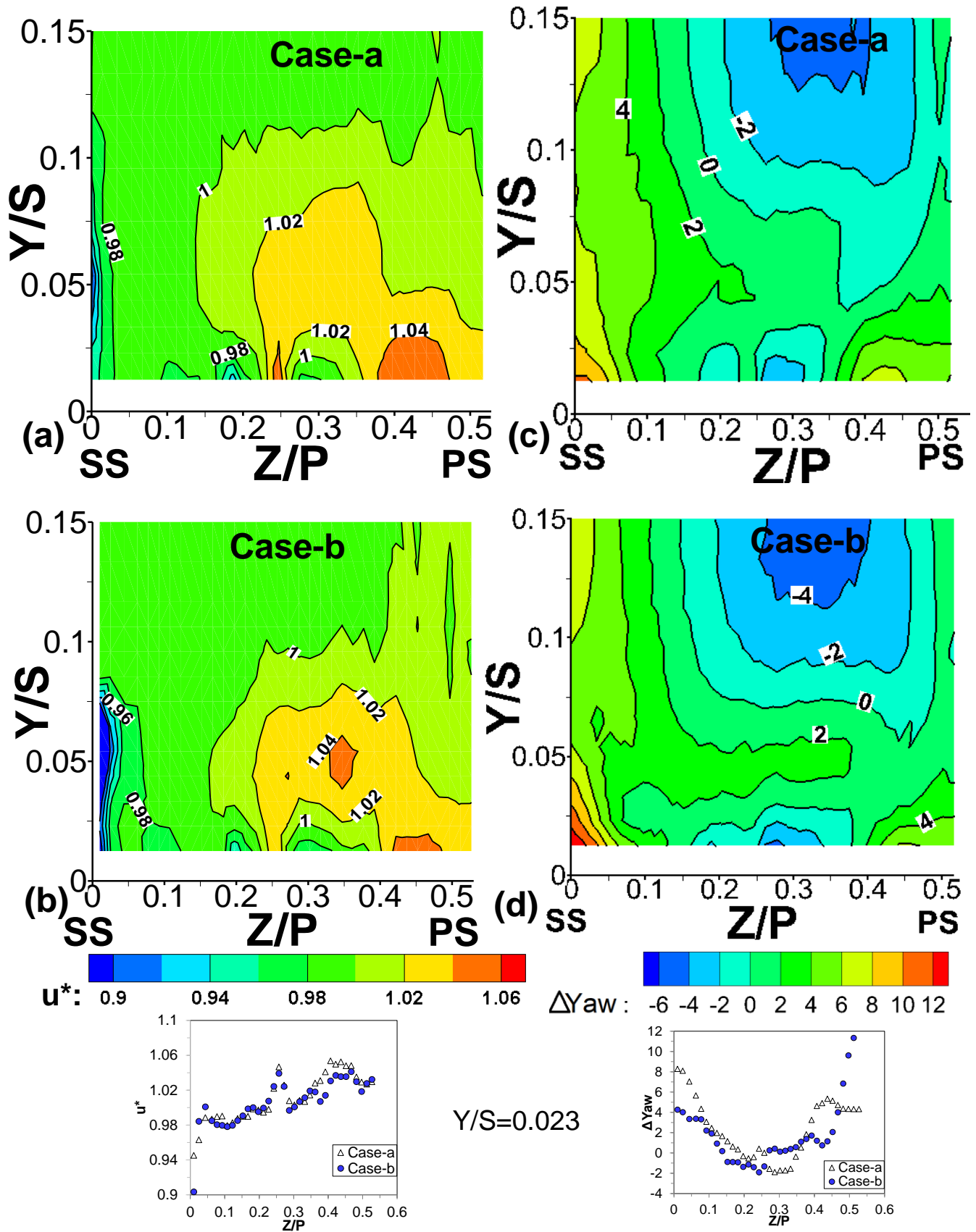
Fig. 13 Distributions of streamline velocity ratio, u* (a, b) and flow yaw-angle deviation (deg), ∆Yaw (c, d) near endwall in Plane-3 for Cases-(a, b) at M=2.2. Data in line plots at the bottom are shown at location Y/S=0.023.
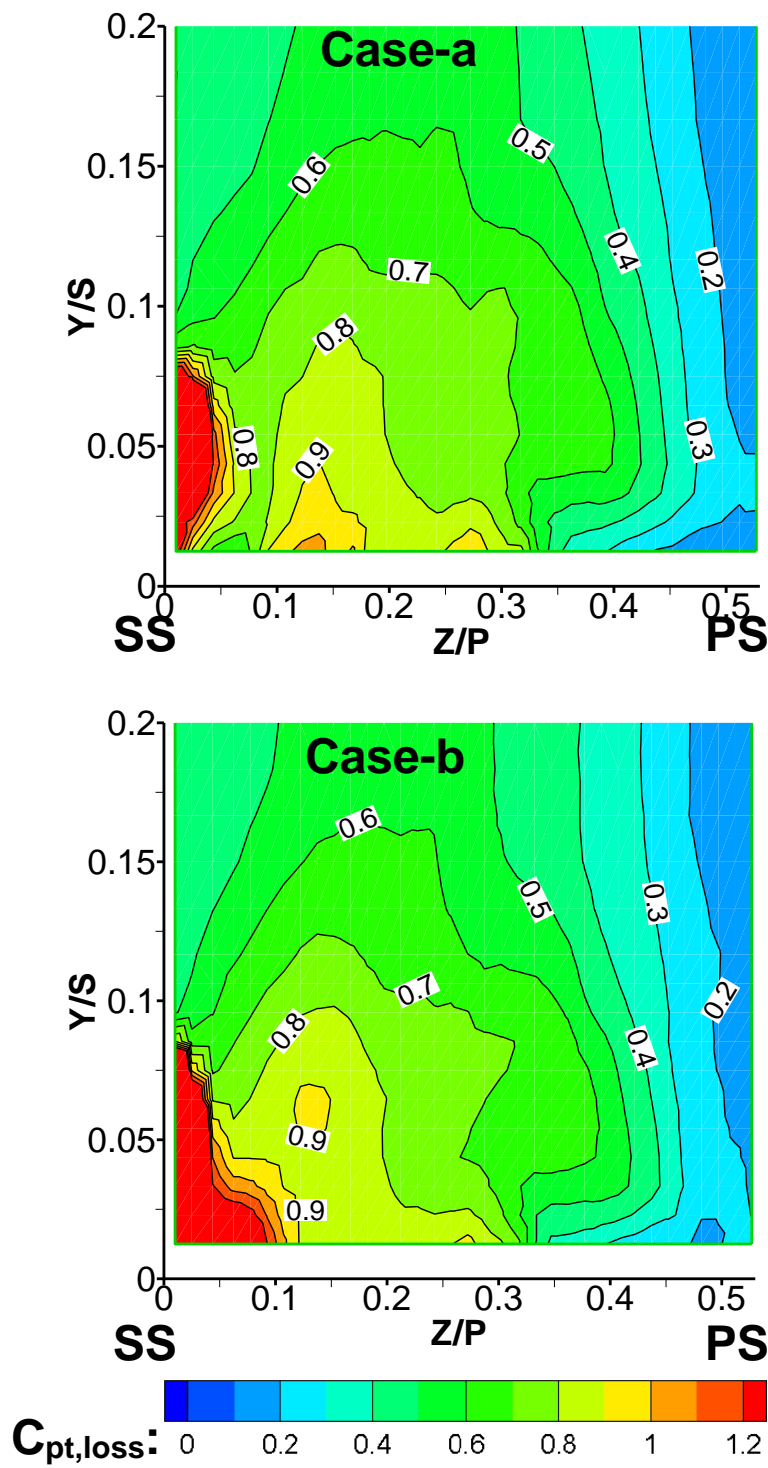
Fig. 14 Distributions of total-pressure loss coefficient, $C_{pt,loss}$ in Plane-3 for Cases-(a, b) at M=1.8.
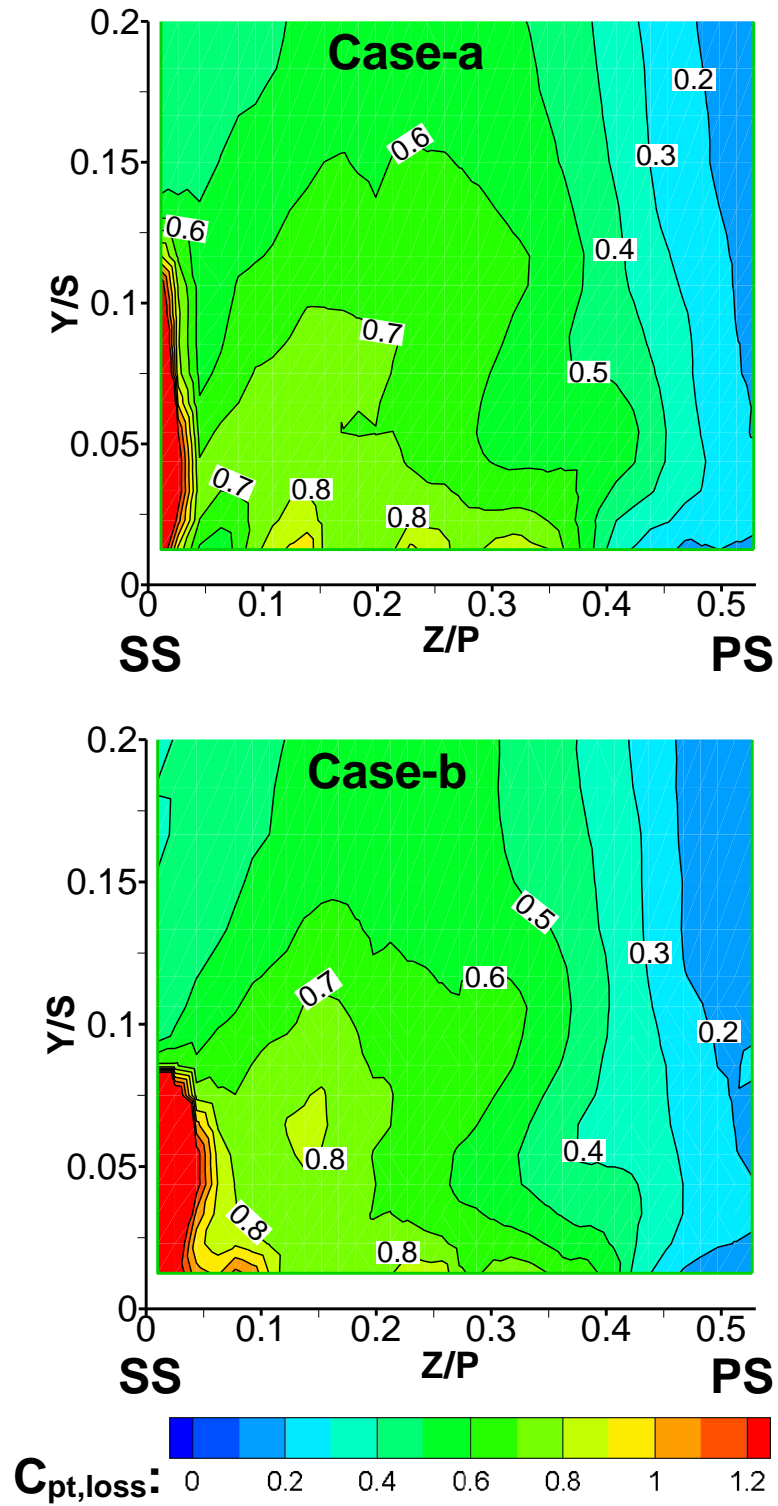
Fig. 15 Distributions of total-pressure loss coefficient, C$_{pt,loss}$ in Plane-3 for Cases-(a, b) at M=2.2.
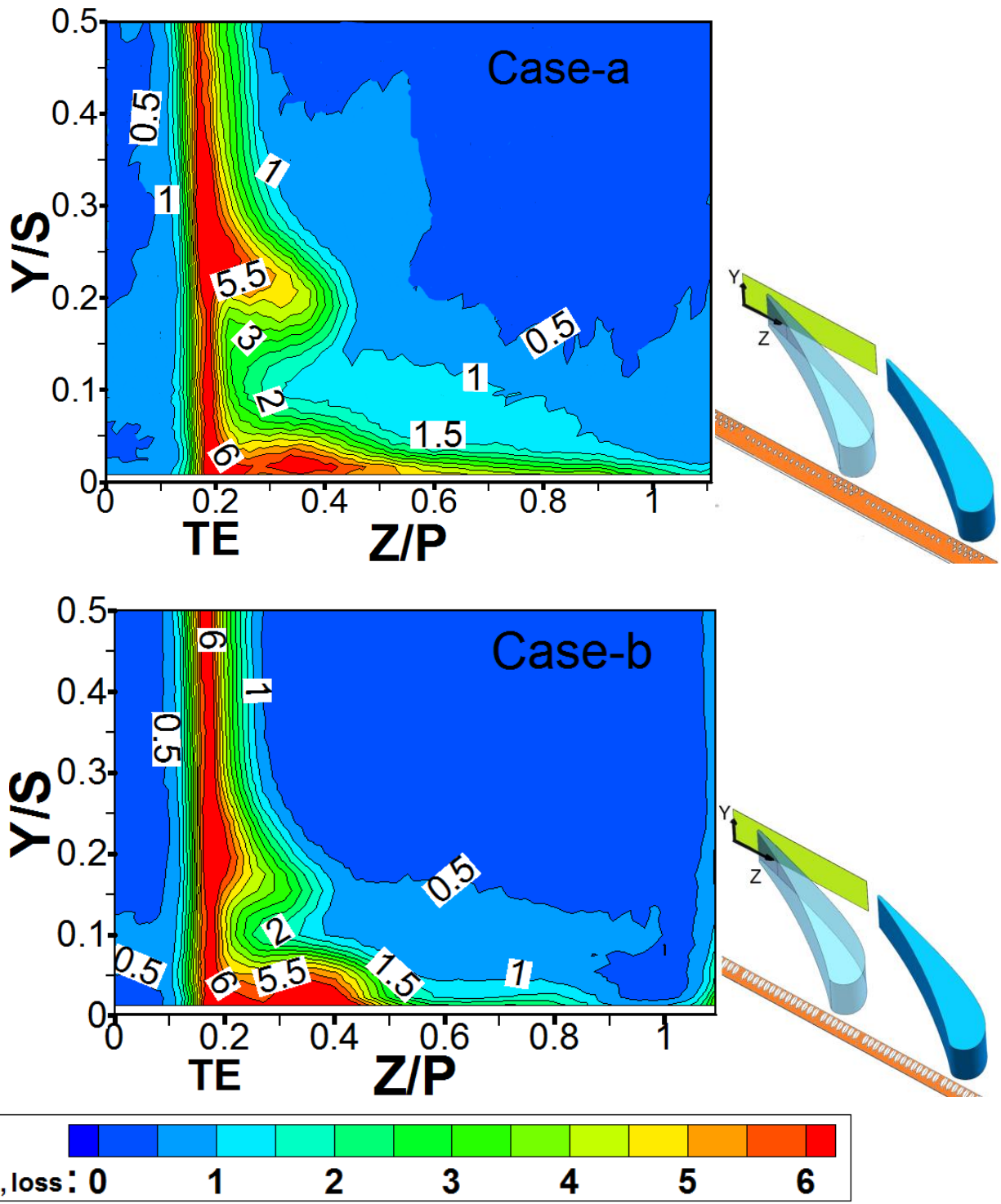
Fig. 16 Distributions of total-pressure loss coefficient, $C_{pt,loss}$ in Plane-4 for Cases-(a, b) at M=2.2.
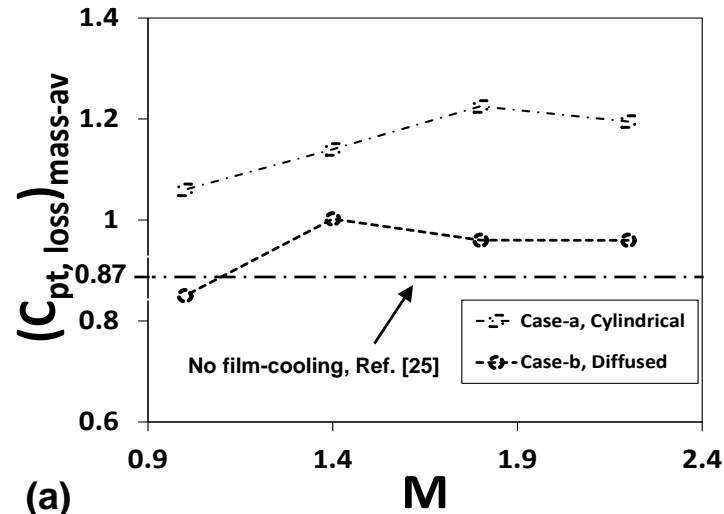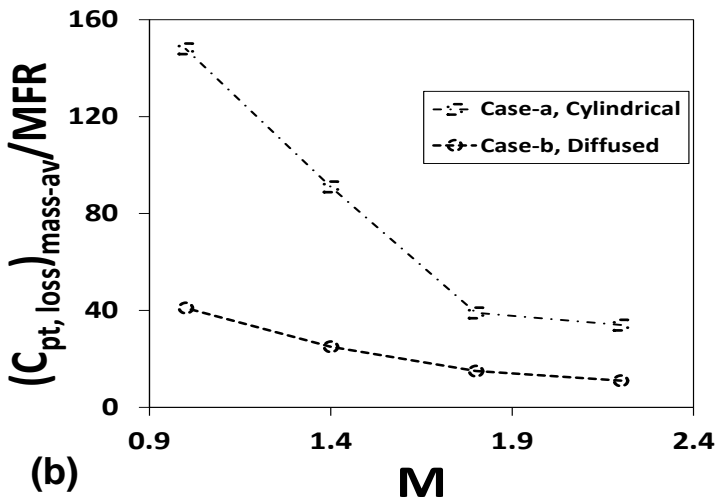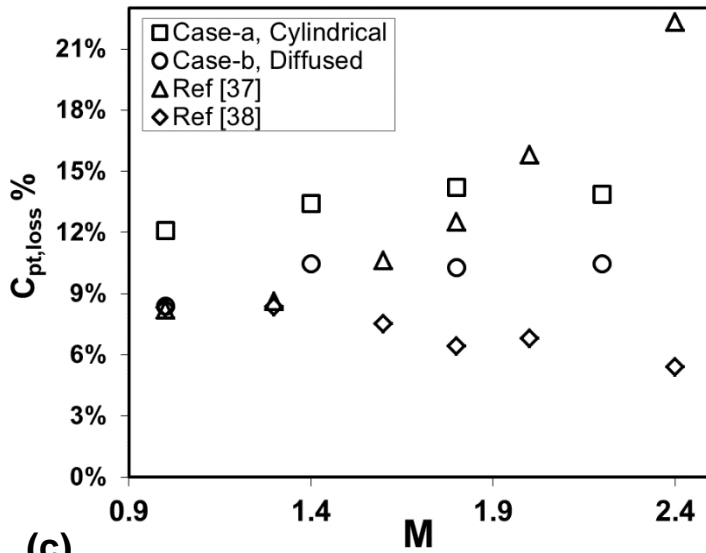
Fig. 17 Comparisons of mass-averaged total-pressure loss coefficients in Plane-4 as blowing ratio, M varies: (a) $(C_{pt,loss})_{mass-av}$, (b) ratios of mass-averaged coefficients to coolant mass fractions, $(C_{pt,loss})_{mass-av}$/MFR, and (c) Overall cascade loss in % with literature data [37, 38].
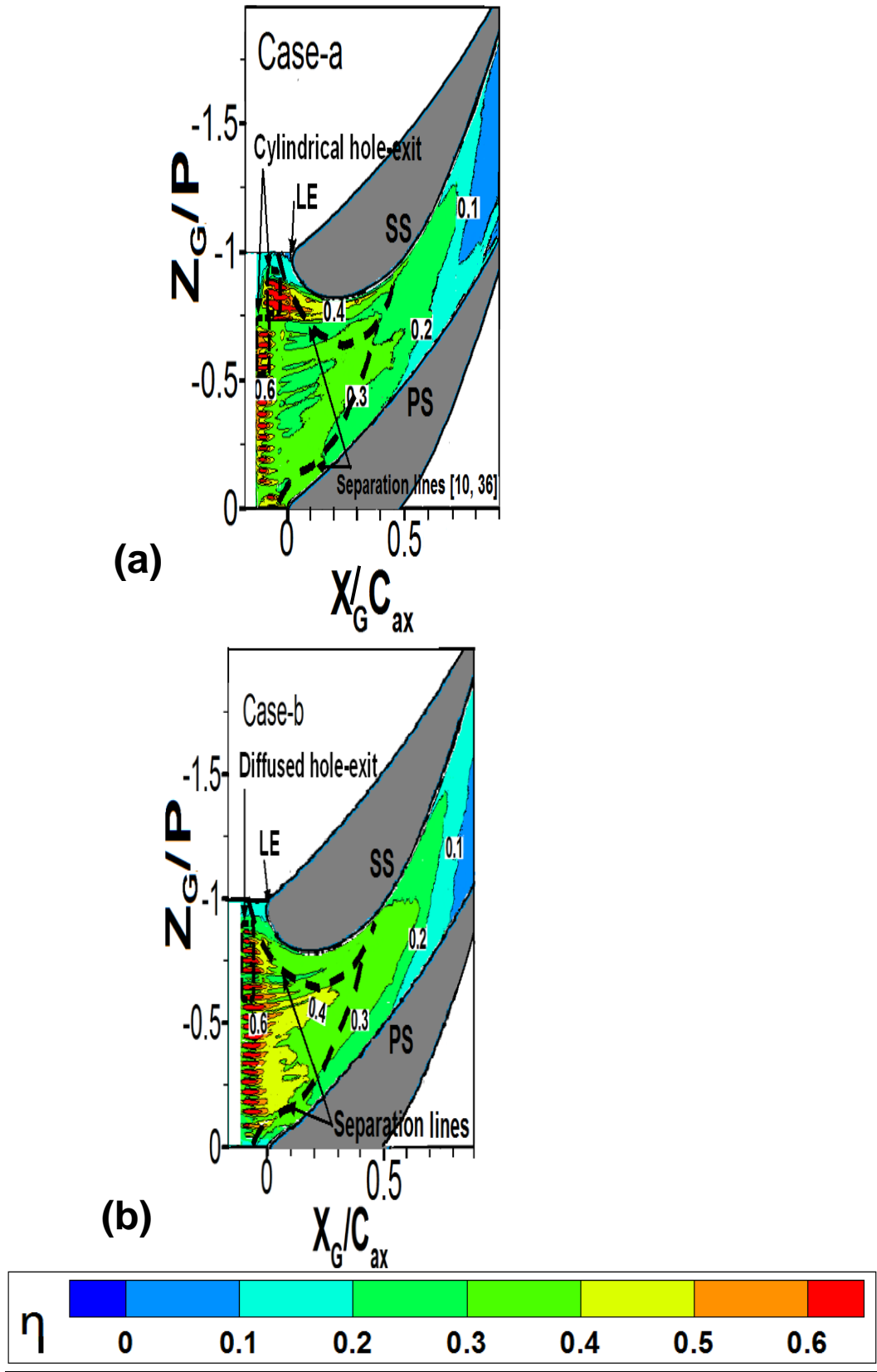
Fig. 18 Distributions of adiabatic film-cooling effectiveness, η along endwall for Cases-(a, b) at M=1.8. Locations of approximate separation lines are based on Refs. [10, 36].
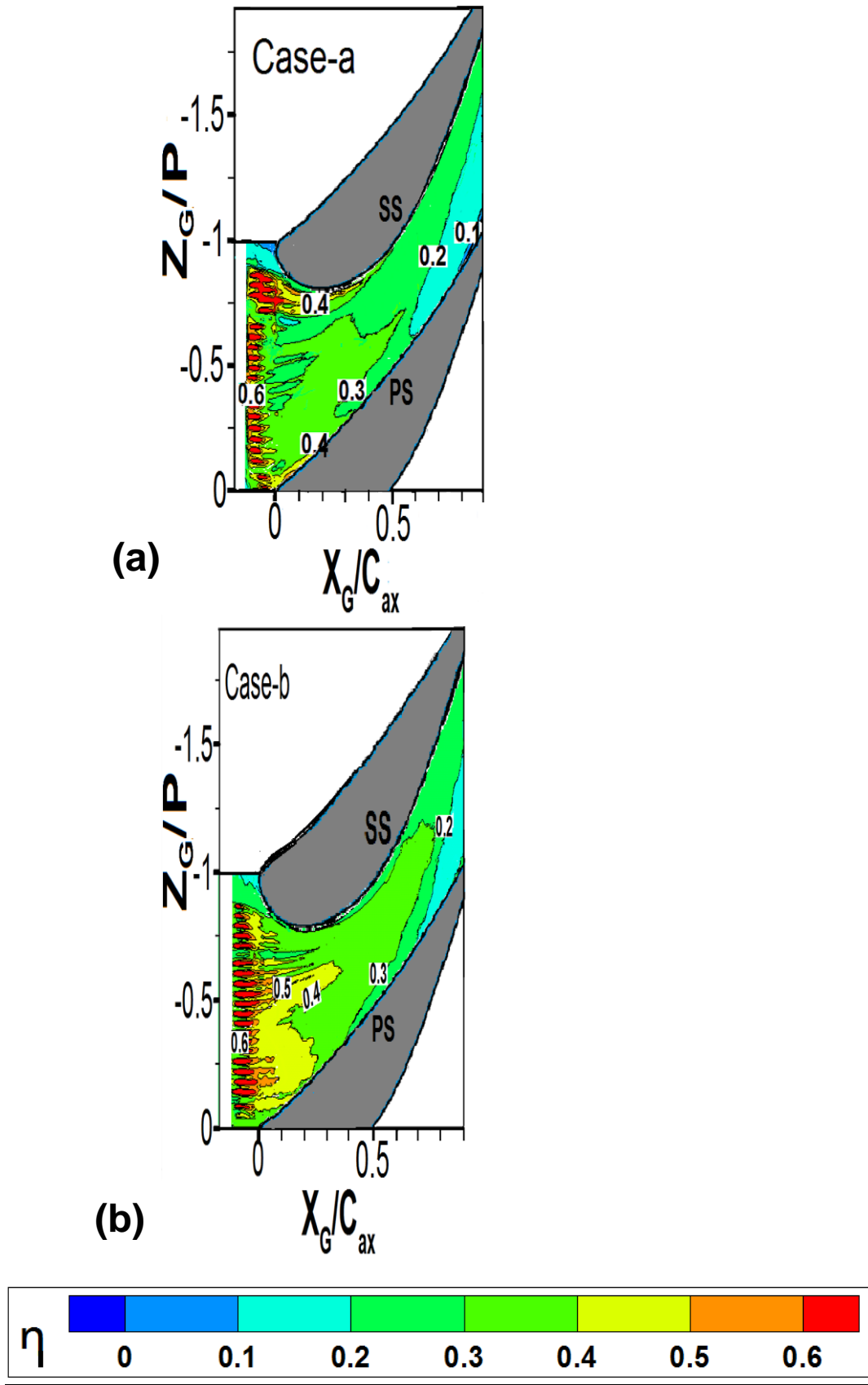
Fig. 19 Distributions of adiabatic film-cooling effectiveness, η along endwall for Cases-(a, b) at M=2.2.
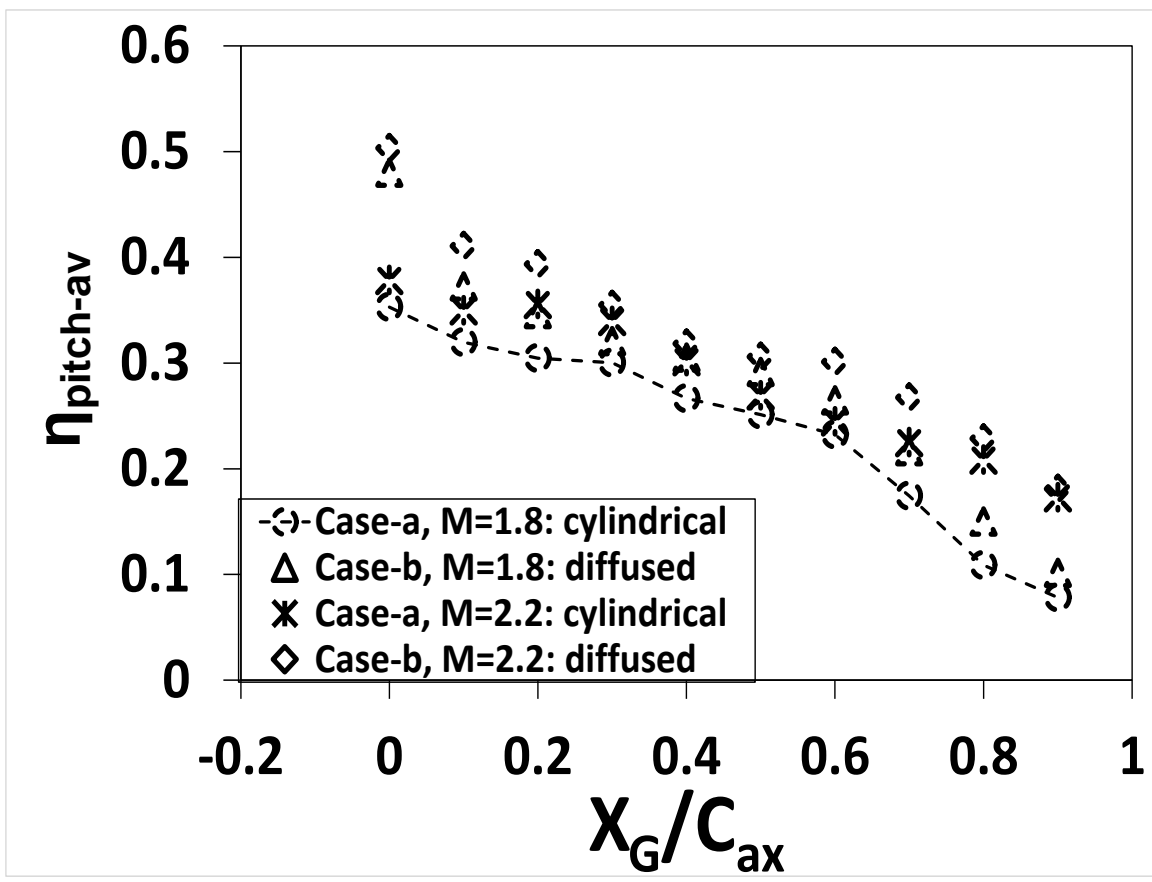
Fig. 20 Pitchwise-averaged film-cooling effectiveness, $\eta_{pitch-av}$ along axial distance, X_G/C_{ax} for Cases-(a, b) at M=1.8 and 2.2.
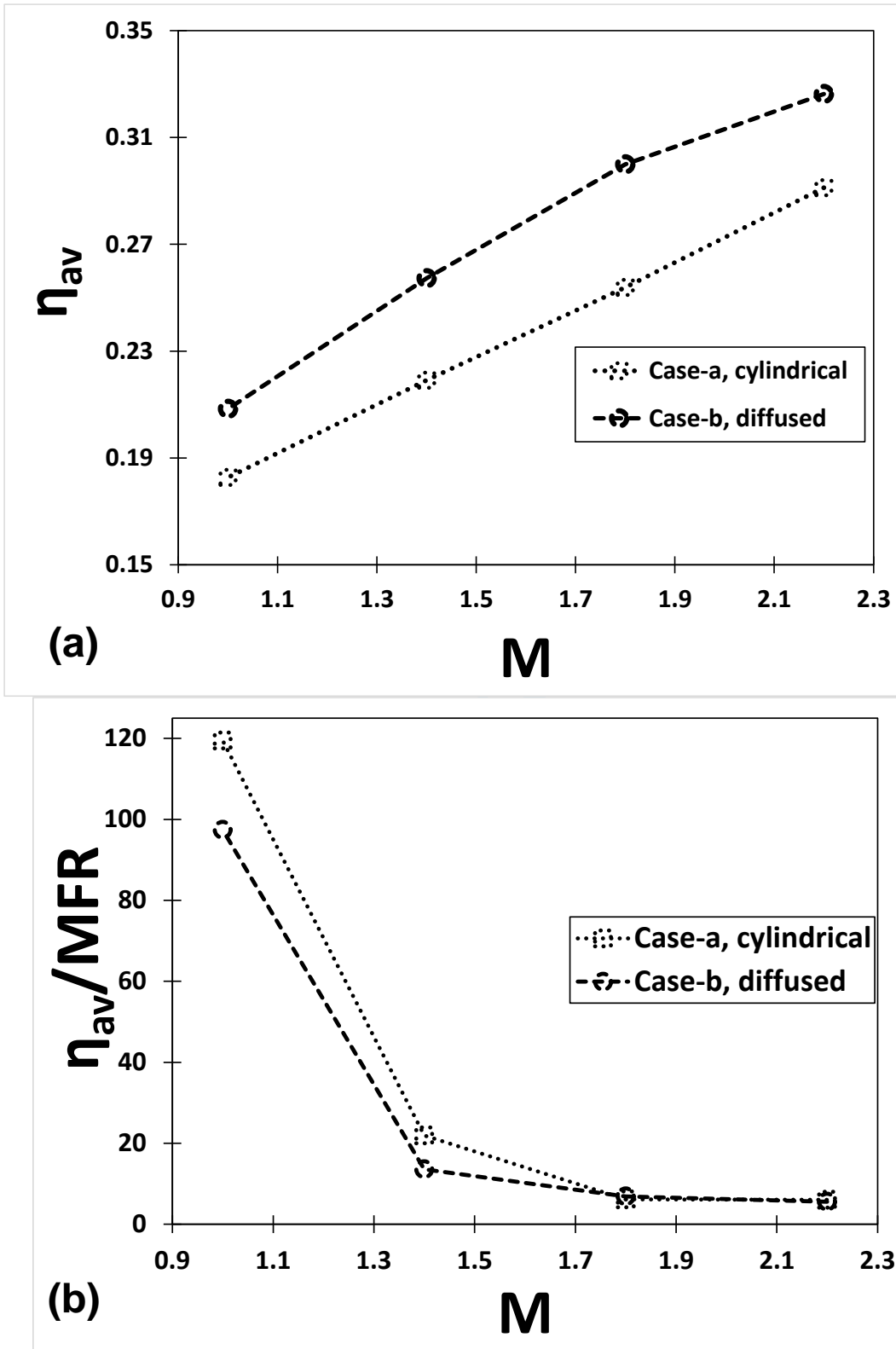
Fig. 21 Comparisons of globally-averaged film-cooling effectiveness as blowing ratio, M varies: (a) η_{av} and (b) ratio of average effectiveness to coolant mass fraction, η_{av}/MFR.
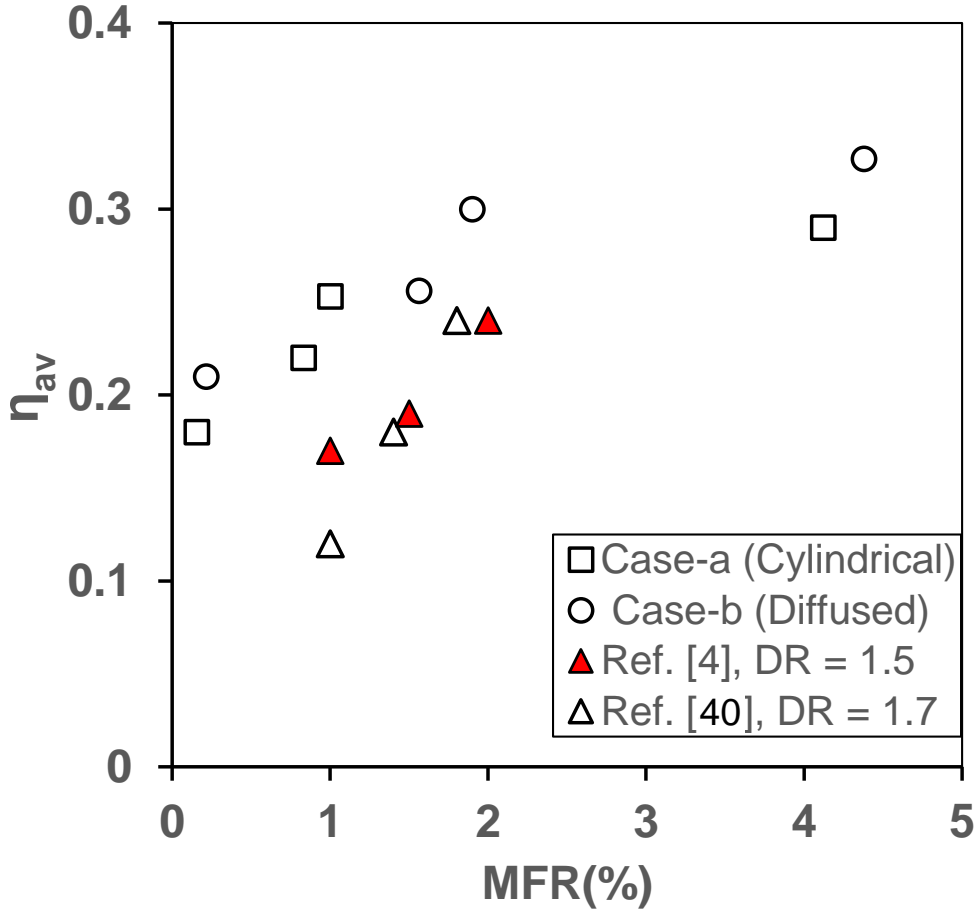
Fig. 22 Comparisons of globally-averaged film-cooling effectiveness with literature data in Refs. [4, 40] as coolant mass fraction, MFR varies. DR = coolant-to-mainstream flow density ratio.